

# Repository of the Max Delbrück Center for Molecular Medicine (MDC) in the Helmholtz Association

https://edoc.mdc-berlin.de/24609/

## Amplification of autoimmune organ damage by NKp46-activated ILC1

Biniaris-Georgallis S.I., Aschman T., Stergioula K., Schreiber F., Jafari V., Taranko A., Karmalkar T., Kasapi A., Lenac Rovis T., Jelencic V., Bejarano D.A., Fabry L., Papacharalampous M., Mattiola I., Molgora M., Hou J., Hublitz K.W., Heinrich F., Guerra G.M., Durek P., Patone G., Lindberg E.L.H., Maatz H., Hölsken O., Krönke G., Mortha A., Voll R.E., Clarke A.J., Hauser A.E., Colonna M., Thurley K., Schlitzer A., Schneider C., Stamatiades E.G., Mashreghi M.F., Jonjic S., Hübner N., Diefenbach A., Kanda M., Triantafyllopoulou A.

This is the final version of the accepted manuscript. The original article has been published in final edited form in:

**Nature** 

2024 OCT 24 ; 634(8035): 952-960

2024 AUG 13 (first published online: final version)

doi: 10.1038/s41586-024-07907-x

URL: https://www.nature.com/articles/s41586-024-07907-x

Publisher: Nature (Springer Nature)

Copyright © The Author(s), under exclusive licence to Springer Nature Limited 2024.

## Publisher's Notice

This is a post-peer-review, pre-copyedit version of an article published in *Nature*. The final authenticated version is available online at https://doi.org/10.1038/s41586-024-07907-x.

## Amplification of autoimmune organ damage by NKp46-activated ILC1

2

1

- 3 Stylianos-Iason Biniaris-Georgallis<sup>1,2,3,4,5,23</sup>, Tom Aschman<sup>1,2,3,6,7,23</sup>, Katerina Stergioula<sup>1,2,3,4,23</sup>,
- 4 Frauke Schreiber<sup>1,2,3</sup>, Vajiheh Jafari<sup>1,2,3</sup>, Anna Taranko<sup>1,2,3</sup>, Tejal Karmalkar<sup>1,2,3,4</sup>, Ana Kasapi<sup>1,2,3</sup>,
- 5 Tihana Lenac Rovis<sup>8</sup>, Vedrana Jelencic<sup>8</sup>, David A. Bejarano<sup>9</sup>, Lea Fabry<sup>1,2,3</sup>, Michail
- 6 Papacharalampous<sup>6</sup>, Irene Mattiola<sup>2,3</sup>, Martina Molgora<sup>10,11</sup>, Jinchao Hou<sup>10,12</sup>, Karolin W.
- 7 Hublitz<sup>3</sup>, Frederik Heinrich<sup>2</sup>, Gabriela Maria Guerra<sup>2</sup>, Pawel Durek<sup>2</sup>, Giannino Patone<sup>13</sup>, Eric
- 8 Lars-Helge Lindberg<sup>13</sup>, Henrike Maatz<sup>13,14</sup>, Oliver Hölsken<sup>2,3,15</sup>, Gerhard Krönke<sup>1,2</sup>, Arthur
- 9 Mortha<sup>16</sup>, Reinhard E. Voll<sup>6</sup>, Alexander J Clarke<sup>17</sup>, Anja E. Hauser<sup>1,2</sup>, Marco Colonna<sup>10</sup>, Kevin
- 10 Thurley<sup>2,18</sup>, Andreas Schlitzer<sup>9</sup>, Christoph Schneider<sup>19</sup>, Efstathios G. Stamatiades<sup>3</sup>, Mir-Farzin
- 11 Mashreghi<sup>2,20</sup>, Stipan Jonjic<sup>8</sup>, Norbert Hübner<sup>13,14,21</sup>, Andreas Diefenbach<sup>2,3,24,\*</sup>, Masatoshi
- 12 Kanda<sup>13,22,24,\*</sup>, and Antigoni Triantafyllopoulou<sup>1,2,3,24,\*</sup>

- <sup>1</sup>Department of Rheumatology and Clinical Immunology, Charité-Universitätsmedizin Berlin,
- 15 Campus Mitte, Berlin, Germany
- <sup>2</sup> German Rheumatism Research Center, A Leibniz Institute, Berlin, Germany
- 17 <sup>3</sup>Institute of Microbiology, Infectious Diseases and Immunology (I-MIDI), Charité-
- 18 Universitätsmedizin Berlin, Campus Benjamin Franklin, Berlin, Germany
- 19 <sup>4</sup>Department of Biology, Chemistry and Pharmacy, Free University of Berlin, Germany
- 20 <sup>5</sup>Current address: Department of Nephrology and Medical Intensive Care, Charité-
- 21 Universitätsmedizin, Berlin, Campus Mitte, Berlin, Germany
- <sup>6</sup>Department of Rheumatology and Clinical Immunology, Medical Center University of Freiburg,
- Faculty of Medicine, University of Freiburg, Freiburg, Germany

- <sup>7</sup>Current address: Department of Neuropathology, Charité-Universitätsmedizin Berlin, Campus
- 25 Mitte, Berlin, Germany
- <sup>8</sup>Center for Proteomics, Faculty of Medicine, University of Rijeka, Rijeka, Croatia
- <sup>9</sup>Quantitative Systems Biology, Life and Medical Sciences (LIMES) Institute, University of Bonn,
- 28 Bonn, Germany
- 29 <sup>10</sup>Department of Pathology and Immunology, Washington University School of Medicine, St.
- 30 Louis, Missouri, MO, USA
- 31 <sup>11</sup>Current address: H.Lee Moffitt Cancer Center & Research Institute, Department of
- 32 Immunology, 12902 USF Magnolia Drive, Tampa FL 33612-9416.
- 33 <sup>12</sup>Current address: Department of Anesthesiology, Children's Hospital, Zhejiang University
- 34 School of Medicine, National Clinical Research Center for Child Health, Hangzhou, China
- 35 <sup>13</sup>Cardiovascular and Metabolic Sciences, Max Delbrück Center for Molecular Medicine in the
- 36 Helmholtz Association (MDC), Berlin, Germany
- 37 <sup>14</sup>DZHK (German Centre for Cardiovascular Research), Partner Site Berlin; Berlin, Germany
- 38 <sup>15</sup>Current address: Department of Anesthesiology and Intensive Care Medicine, Charité –
- 39 Universitätsmedizin Berlin, Berlin, Germany; BIH Academy, Clinician Scientist Program,
- 40 Charitéplatz 1, 10117 Berlin, Germany
- 41 <sup>16</sup>Department of Immunology, University of Toronto, Toronto, ON, Canada
- 42 <sup>17</sup>Kennedy Institute of Rheumatology, University of Oxford, Oxford, UK
- 43 <sup>18</sup>Biomathematics Division, Institute of Experimental Oncology, University Hospital Bonn, Bonn,
- 44 Germany
- 45 <sup>19</sup>Institute of Physiology, University of Zurich, Zurich, Switzerland
- 46 <sup>20</sup>German Center for Child and Adolescent Health (DZKJ), partner site Berlin, Berlin Germany.

21Charité Universitätsmedizin, Berlin, Germany
 22Department of Rheumatology and Clinical Immunology, Sapporo Medical University
 School of Medicine, Sapporo, Hokkaido, Japan
 23These authors contributed equally.
 24These authors jointly supervised this work.
 \*Correspondence: antigoni.triantafyllopoulou@charite.de; mkanda@sapmed.ac.jp;
 andreas.diefenbach@charite.de

In systemic lupus erythematosus (SLE) loss of immune tolerance, autoantibody production and immune complex deposition are required but not sufficient for organ damage<sup>1</sup>. How inflammatory signals are initiated and amplified in the setting of autoimmunity remains elusive. Here, we set out to dissect layers and hierarchies of autoimmune kidney inflammation in order to identify tissue-specific cellular hubs that amplify autoinflammatory responses. Using high-resolution single-cell profiling of kidney immune and parenchymal cells, in combination with antibody blocking and genetic deficiency, we show that tissue-resident NKp46<sup>+</sup> innate lymphoid cells (ILC) are crucial signal amplifiers of disease-associated macrophage expansion and epithelial cell injury in lupus nephritis, downstream of autoantibody production. NKp46 signaling in a distinct subset of ILC1 instructed an unconventional immune-regulatory transcriptional program, which included the expression of the myeloid cell growth factor CSF2. CSF2 production by NKp46<sup>+</sup> ILC promoted the population expansion of monocyte-derived macrophages. Blockade of the NKp46 receptor (using the antibody mNCR1.15<sup>2</sup>) or genetic deficiency of NKp46 abrogated epithelial cell injury. The same cellular and molecular patterns were operative in human lupus nephritis. Our data support that NKp46<sup>+</sup> ILC1 promote parenchymal cell injury by granting monocyte-derived macrophages access to epithelial cell niches. NKp46 activation in ILC1 thus constitutes a previously unrecognized, critical tissue rheostat that amplifies organ damage in autoimmune hosts, with broad implications for inflammatory pathologies and therapies.

77

57

58

59

60

61

62

63

64

65

66

67

68

69

70

71

72

73

74

75

76

78

Lupus nephritis is a major cause of morbidity and mortality in SLE, an autoimmune disease that predominantly affects young women. Clinical data show that while most SLE patients have autoantibodies, not all develop severe inflammatory disease. Thus, breach of immunological tolerance *per se* may not be sufficient to initiate full blown inflammation and tissue damage<sup>1</sup>. This raises the important question of how inflammatory signals are initiated and amplified in autoimmune diseases. Given their immune-regulatory role in various tissues<sup>3</sup>, we considered that kidney tissue-resident ILC may be a central rheostat of the inflammatory spiral, conferring differential susceptibility of SLE patients to severe disease and organ damage.

Similar to human SLE, female NZB/W F1 mice develop type I IFN-driven disease<sup>4</sup>.

## Tissue NKp46<sup>+</sup> ILC increase in numbers in lupus nephritis

Administration of poly(I:C) synchronizes disease onset, while concurrent treatment with blocking antibodies to IFNAR1 suppresses disease (Extended Data Fig. 1a-b). To discriminate between leukocytes in the kidney tissue and those in the kidney vasculature, we injected NZB/W F1 mice with fluorescently-labelled CD45 antibodies intravenously (*i.v.*) directly before analysis. Leukocytes within vessels (vessel-associated) were CD45*i.v.*<sup>+</sup>, whereas leukocytes in tissues were CD45*i.v.*-negative. Type I IFNs induced a significant increase in tissue leukocytes (Extended Data Fig. 1c).

ILC1, NKp46<sup>+</sup> ILC3 and conventional NK cells<sup>5</sup> express the activating immunoreceptors NKp46 and NK1.1 and are here collectively referred to as NKp46<sup>+</sup> ILC (Lin<sup>-</sup> NKp46<sup>+</sup> NK1.1<sup>+</sup> cells). CD49b (integrin α2) and Eomes are expressed by NK cells but not by CD49b<sup>-</sup> ILC1 or ILC3<sup>5</sup>. In kidneys from young NZB/W F1 mice, vessel-associated cells were Eomes<sup>+</sup> CD49b<sup>+</sup> (Fig. 1a, Extended Data Fig. 1d), whereas tissue cells were Eomes<sup>-</sup> CD49b<sup>-</sup>. Strikingly, an increase in

tissue NKp46<sup>+</sup> ILC (both, CD49b<sup>+</sup> and CD49b<sup>-</sup> cells) was observed in nephritic mice (Fig. 1a). NK cells depend on Eomes, while ILC1 and NKp46<sup>+</sup> ILC3 depend on Gata3<sup>5</sup>. Similarly, poly(I:C) injections into B6 mice increased the representation of CD49b<sup>+</sup> and CD49b<sup>-</sup> tissue NKp46<sup>+</sup> ILC (Extended Data Fig. 1f-g). CD49b<sup>+</sup> cells were >95% reduced in *Ncr1*<sup>Cre/+</sup>; *Eomes*<sup>fl/fl</sup> mice, while CD49b<sup>-</sup> CD45*i.v.*<sup>-</sup> tissue cells were not significantly affected. In contrast, CD49b<sup>+</sup> NK cells were maintained in poly(I:C)-treated *Ncr1*<sup>Cre/+</sup>; *Gata3*<sup>fl/fl</sup> mice, but tissue CD49b<sup>-</sup> cells were significantly reduced in numbers. Thus, CD49b<sup>+</sup> NKp46<sup>+</sup> ILC are NK cells and tissue CD49b<sup>-</sup> NKp46<sup>+</sup> cells are ILC1 or NKp46<sup>+</sup> ILC3.

## NKp46<sup>+</sup> ILC control autoimmune organ damage

We addressed the role of NKp46<sup>+</sup> ILC in lupus nephritis. While short-term injection of antiasialoGM1, known to target NK cells<sup>6</sup> and NKp46<sup>+</sup> ILC<sup>7</sup>, effectively depleted both tissue and vessel-associated NKp46<sup>+</sup> ILC (data not shown), extended treatment with anti-asialoGM1 (Extended Data Fig. 1h) significantly reduced tissue but not vessel-associated NKp46<sup>+</sup> ILC (Fig. 1a). Remarkably, extended anti-asialoGM1 treatment significantly ameliorated lupus nephritis shown by reduced proteinuria and serum blood urea nitrogen (BUN) levels (Fig. 1b, Extended Data Fig. 1i), but did not affect serum anti-dsDNA antibody titers (Fig. 1c). Anti-asialoGM1 treatment also ameliorated spontaneous lupus nephritis (Extended Data Fig. 1j-k).

To selectively target NKp46<sup>+</sup> ILC and to explore the role of NKp46 signaling, we injected NZB/W F1 mice with blocking antibodies to the activating immunoreceptor NKp46 (clone mNCR1.15)<sup>2</sup> (Fig. 1d-e, Extended Data Fig. 2a-c). Short-term mNCR1.15 treatment did not deplete NKp46<sup>+</sup> ILC (Extended Data Fig. 2d-e). Rather, mNCR1.15 showed blocking activity in conventional killing assays and binding assays using recombinant NKp46 fusion proteins and

ligand-expressing target cells (Extended Data Fig. 2f-h). Blockade of NKp46 improved parameters of kidney damage (BUN levels) and prevented the increased expression of *Hayer1*, encoding KIM-1, a marker of tubular injury (Fig. 1d) and the population expansion of tissue NKp46<sup>+</sup> ILC (Extended Data Fig. 2c). Serum anti-dsDNA titers were unaffected (Fig. 1e). Thus, NKp46 signaling controls autoimmune kidney damage. To explore the effect of NKp46<sup>+</sup> ILC depletion on the kidney parenchyma, we performed single cell RNA-sequencing (scRNA-seq) of whole kidneys of lupus-prone mice (Fig. 1f, Extended Dat Fig. 3a-c, Supplementary Table 1), including groups depleted of tissue NKp46<sup>+</sup> ILC. We analyzed podocytes, since podocyte injury leads to proteinuria<sup>8</sup>. After subsetting parietal epithelial cell (PEC)/podocyte clusters (Fig. 1g-h), we identified podocytes, based on expression of podocytespecific transcripts (Fig. 1i, Extended Data Fig. 3d-e). Podocyte cluster Pod2 was substantially underrepresented in lupus nephritis (Fig. 1h, Extended Data Fig. 3f), reflecting extensive podocyte injury. This was prevented by depletion of tissue NKp46<sup>+</sup> ILC. PEC react to glomerular injury by forming cellular crescents<sup>9</sup>. Flat PEC (fPEC) cover the Bowman's capsule, while intermediate PEC (iPEC) are a transitional population between fPEC and proximal tubular cells<sup>9</sup>. We observed reduced representation of homeostatic fPEC and an expansion of lupus nephritis (LN)-associated clusters LN-iPEC1, LN-iPEC2, LN-iPEC3, and LNfPEC (Fig. 1h, Extended Data Fig. 3f), changes that were abrogated by depleting tissue NKp46<sup>+</sup> ILC. An unbiased analysis of differentially co-regulated genes across PEC/podocytes revealed three modules (Fig. 1j). Module 1 comprised of genes belonging to iPEC/LN-iPEC, module 2 included typical podocyte marker genes and module 3 consisted of genes derived from fPEC/LNfPEC. Module 1 contained Cd44, a marker of activated iPEC<sup>10</sup>, Cd9, required for the oriented migration of PECs<sup>11</sup>, chemokine transcripts (Ccl2, Ccl5, Cxcl16, and Cxcl1), and Il34, encoding a

126

127

128

129

130

131

132

133

134

135

136

137

138

139

140

141

142

143

144

145

146

147

ligand for macrophage colony stimulating factor receptor (CSF1R). LN-iPEC were particularly enriched in transcripts reflecting immune cell functions (e.g., Ccl2, Ccl5, Il34, H2-Aa, H2-Ab1) or epithelial cell injury (Haverl) and fibrosis (e.g. Pdgfa). A similar transcriptional program related to epithelial activation was expressed by a cluster of proximal tubular epithelial cells (LN-PT) (Extended Data Fig. 3g-j). Analysis of module 3 revealed a mesenchymal cell state, promoting extracellular matrix remodeling and a pro-fibrotic response (e.g. Acta2, Fn1, Pdfgrb) (Fig. 1j). Module 3 transcripts were significantly enriched in LN-fPEC (Fig. 1k). Epithelial cells within cellular crescents, in close contact with F4/80<sup>+</sup> macrophages, expressed smooth muscle actin ( $\alpha$ -SMA), a marker of fibrosis encoded by Acta2, and the iPEC activation marker CD44 (Fig. 11). Both histological and transcriptional disease-associated changes were reversed by tissue NKp46<sup>+</sup> ILC depletion (Fig. 1h,i,l) or NKp46 blocking (Fig. 1m). In lupus nephritis, immune complexes deposit in glomerular capillaries. Capillary (cEC) and glomerular capillary (gEC) endothelial cells<sup>12</sup> (Extended Data Fig. 4a-d) from nephritic kidneys had reduced expression of typical endothelial cell markers, including *Plvap* and markers associated with VEGF signaling and vessel growth, such as Nrp1 (encoding neuropilin 1), Kdr (encoding VEGF receptor 2), and Esm1 (encoding endothelial cell specific molecule 1) (Extended Data Fig. 4e-f). Further, they expressed higher levels of genes related to pathological angiogenesis (i.e., Lgr1)<sup>13</sup>, profibrotic and stress responses (i.e., Col4a1, Col4a2, Serpine2, Mt1)<sup>14,15</sup>. These transcriptional changes were reversed by tissue NKp46<sup>+</sup> ILC depletion. Pathways related to physiological angiogenesis were downregulated in cEC and gEC from nephritic kidneys, while profibrotic pathways and IFN responses were upregulated (Extended Data Fig. 4g-h).

149

150

151

152

153

154

155

156

157

158

159

160

161

162

163

164

165

166

167

168

169

Three small EC clusters were overrepresented in lupus nephritis (clusters LN-EC1, LN-EC2, LN-EC3). LN-EC1 and LN-EC2 had reduced levels of typical cEC or gEC markers (Extended Data Fig. 4b-d), and increased levels of transcripts related to oxidative stress (e.g., Gpx3 and *Ucp2*)<sup>16,17</sup>. LN-EC3 were enriched in genes related to replication stress (i.e., *Rrm2*, *Brca1*, *Brca2*, Ccna2, Ccnb1, and E2f2) (Extended Data Fig. 4i)<sup>18</sup>. Overall, the data are consistent with capillary EC injury and a profibrotic response. Immunofluorescence showed extensive remodeling of peritubular cECs and capillary loops in nephritic glomeruli, reversed by tissue NKp46<sup>+</sup> ILC depletion (Extended Data Fig. 4j). Thus, blockade of NKp46 or depletion of tissue NKp46<sup>+</sup> ILC reversed podocyte loss, capillary endothelial cell injury, and expansion of LN-associated iPECs. To test the role of NKp46 signaling in lupus nephritis using mouse genetics, we treated BALB/c mice with imiquimod (a TLR7 agonist), thus inducing lupus-like nephritis<sup>27</sup>. NKp46-deficient  $(Ncr I^{-1/-})$  BALB/c mice had significantly reduced proximal tubular damage (i.e. reduced expression of KIM-1, encoded by *Haver1*) and were protected from kidney failure (i.e., elevated serum BUN levels) (Fig. 1n-p). Collectively, data from two mouse SLE models, using antibody blockade and gene targeting, demonstrate that autoimmune tissue damage requires operative NKp46 signaling and tissue NKp46<sup>+</sup> ILC.

187

188

189

190

191

192

186

171

172

173

174

175

176

177

178

179

180

181

182

183

184

185

#### An immunoregulatory program instructed by NKp46

We analyzed tissue NKp46<sup>+</sup> ILC by scRNA-seq (Extended Data Fig. 5a-b, <u>Supplementary Table 2</u>), including tissue NK1.1<sup>+</sup> ILC from mice treated with NKp46 blocking antibodies. Tissue NKp46<sup>+</sup> ILC could be divided into tILC (ILC1 and NKp46<sup>+</sup> ILC3) and tNK (tissue NK cells). tILC expressed high levels of ILC1- (e.g., *Thy1*, *Cxcr6*, *Cd226*, *Tbx21*) but low levels of NK-related

193 genes (e.g., Eomes, granzymes, and Klra genes, encoding Ly49 receptors) (Fig. 2a-b, Extended 194 Data Fig. 5c-d). 195 Two tNK clusters were enriched in nephritis (Extended Data Fig. 5a): Tcf7+ tNK expressed 196 Tcf7 and Eomes consistent with an early state of NK cell differentiation<sup>19</sup>, Tigit<sup>+</sup> tNK expressed 197 higher levels of *Tigit* but lower levels of *Tbx21*, *Gzma*, and *Prf1* (Extended Data Fig. 5d-e). TIGIT 198 has been linked to NK cell exhaustion<sup>20</sup>. Tigit<sup>+</sup> tNK also expressed Lgals<sup>3</sup>, encoding Galectin 3, 199 has inhibitory effects in human NK cells<sup>21</sup>. Thus, Tigit<sup>+</sup> tNK may represent a 200 "dysfunctional" NK cell state<sup>22</sup>. In agreement, tNK cells from nephritic kidneys showed very low 201 degranulation in response to target cells when compared to vessel-associated NK cells. The latter 202 retained cytotoxic potential, albeit at lower levels than splenic NK cells (Extended Data Fig. 5f). Zfp683+ (Zfp683 encodes Hobit) and Il7r+ tILC likely represented mature and immature ILC1 203 204 clusters<sup>23,24</sup>: Zfp683<sup>+</sup> tILC expressed higher levels of Zfp683, Cxcr6, Cd226, Tnfsf10, Gzma, and 205 Prf1, while Il7r<sup>+</sup> tILC expressed higher levels of Il7r, Il18r1, Ikzf2, and Cd160 (Fig. 2b, Extended 206 Data Fig. 5c-e). Il2+ tILC were enriched in nephritic kidneys (Extended Data Fig. 5a) and 207 expressed higher levels of transcripts associated with an immature ILC state (Tcf7, Il7r) or ILC 208 activation and proliferation (*Gzmc*, *Il2*) (Fig. 2b, Extended Data Fig. 5e). 209 We identified a cluster, annotated as *Tnfrsf9*<sup>+</sup> tILC, with unique characteristics setting them 210 apart from Hobit-expressing ILC1 and suggesting an immune-regulatory role: while expressing 211 canonical ILC genes (e.g. Cxcr6, Il7r, Ikzf2 and Id2), Tnfrsf9<sup>+</sup> tILC expressed lower levels of 212 Zfp683 but high levels of Il2ra (encoding CD25), TNF superfamily genes (e.g. Tnfrsf1b encoding 213 TNF receptor 2, Tnfrsf9 encoding 4-1BB, Lta encoding Lymphotoxin a, Tnfsf14 encoding 214 LIGHT), class II MHC-related transcripts (i.e. Cd74, H2-Eb1, H2-Aa, H2-Ab1), leukocyte

adhesion molecules (*Icam1*), chemokine (*Ccl1*) and growth factor genes (*Csf1*, *Csf2* and *Tgfb1*)

(Fig. 2b, Extended Data Fig. 5c-e). Prominent were NF-κB target genes (e.g. *Trp53*, *Rel*, *Nfkb2*, *Nfatc1*, *Icam1*, *Tnfrsf9*, *Csf2*) and *Crtam* (class I MHC-restricted T cell-associated molecule), encoding a surface molecule that promotes cytokine transcription and tissue residency in activated T cells<sup>25,26</sup>. *Tnfrsf9*<sup>+</sup> tILC expressed higher levels of *Csf2*, *Tnfrsf9*, and class II MHC molecules in nephritis, suggesting cellular activation (Fig. 2c). Strikingly, *Tnfrsf9*<sup>+</sup> tILC, but not other NKp46<sup>+</sup> ILC clusters, were highly enriched in NKp46 activation-associated genes (Fig. 2d). *Tnfrsf9*<sup>+</sup> tILC were increased in nephritis, in an NKp46-dependent manner (Fig. 2e).

## NKp46<sup>+</sup> tILC in human lupus nephritis

Re-analysis of leukocytes derived from human lupus nephritis biopsies<sup>28</sup>, identified NKp46<sup>+</sup> ILC based on the lack of typical T cell markers and higher expression of *NCR1* and *NCAM1* (clusters CT1 and CT5b, Extended Data Fig. 6a, b). NKp46<sup>+</sup> ILC consisted of one cluster with typical NK cell markers, and a cluster expressing markers of tILC, including lower levels of *GZMB* and *ZEB2*, and higher levels of *XCL1* (Extended Data Fig. 6c). Within the second cluster, a subset of cells expressed higher levels of *KIT*, *IL7R*, *LTB*, *IL1R1*, *AHR* and *RORC*, reminiscent of an ILC3 signature and another subset of cells expressed *CXCR6*, *CXCR3*, *GZMA*, *GZMK* and *ZNF683* (encoding HOBIT), characteristic of ILC1. Thus, NKp46<sup>+</sup> ILC1 and ILC3-like cells are also present in human lupus nephritis.

## NKp46-instructed ILC are ILC1

To assign *Tnfrsf9*<sup>+</sup> tILC to the ILC1 *vs.* ILC3 lineage, we used double reporter mice for Eomes (*Eomes*<sup>Gfp/+</sup>) and RORγt (RORγt-fate map (FM) mice), where cells that expressed RORγt are permanently marked by YFP<sup>5</sup>. Vessel-associated NKp46<sup>+</sup> ILC were mostly Eomes<sup>+</sup> NK cells,

while tissue NKp46<sup>+</sup> ILC at steady-state were mostly Eomes<sup>-</sup> RORγt-FM<sup>-</sup> ILC1. A distinct population of RORγt-FM<sup>+</sup> Eomes<sup>-</sup> ILC was also observed (Extended Data Fig. 6d). Poly(I:C) treatment increased Eomes<sup>+</sup> tNK cells and Eomes<sup>-</sup> NKp46<sup>+</sup> tILC.

We analyzed tissue RORγt-FM<sup>+</sup> and RORγt-FM<sup>-</sup> NKp46<sup>+</sup> ILC by scRNA-seq, including cells from poly (I:C)-treated mice. Similar to nephritic mice, we identified clusters of tILC, tNK cells and a *Tnfrsf9*<sup>+</sup> tILC cluster enriched in NKp46 activation-associated genes (Extended Data Fig. 6e-g, Supplementary Table 3). RORγt-FM<sup>+</sup> and RORγt-FM<sup>-</sup> NKp46<sup>+</sup> ILC did not locate to distinct clusters (Extended Data Fig. 6h). *Tnfrsf9*<sup>+</sup> tILC derived mostly from RORγt-FM<sup>-</sup> ILC, but within *Tnfrsf9*<sup>+</sup> tILC, RORγt-FM<sup>+</sup> expressed higher levels of NKp46 activation-associated genes compared to RORγt-FM<sup>-</sup> cells (Extended Data Fig. 6i-j). We conclude that NKp46 stimulation may lead to temporary activation of RORγt gene expression in NKp46<sup>+</sup> ILC1 coordinating a transcriptional program with some overlap to ILC3.

#### NKp46 amplifies renal injury via CSF2

NKp46<sup>+</sup> tILC showed low cytotoxic activity and did not produce high levels of cytokines that can cause tissue damage. Given the production of CSF2 by NKp46<sup>+</sup> tILC, and the remarkable changes in mononuclear phagocyte dynamics observed in the inflamed kidney<sup>4</sup>, we explored if kidney *Csf2* expression links NKp46<sup>+</sup> ILC to organ damage. NKp46 engagement regulated CSF2 production by ILC1 on the protein level, since CD49b<sup>-</sup> ILC1 but not CD49b<sup>+</sup> NK cells from nephritic mice produced substantial amounts of CSF2 when triggered with NKp46 (Fig. 3a). *Tnfrsf9*<sup>+</sup> tILC were the only source of *Csf2* transcripts among all kidney tILC and tNK subsets and *Csf2* expression depended on NKp46 signaling (Fig. 3b). *Csf2* expression in the kidney was low in healthy controls,

but significantly increased in nephritis in both NZB/W F1 and in the imiquimod model (Fig. 3c). This increase was reversed by depletion of tissue NKp46<sup>+</sup> ILC or *Ncr1* deficiency, respectively. CSF2 blocking antibodies (clone MP1-22E9) substantially reduced proteinuria, serum BUN, accumulation of macrophages, and proximal tubular epithelial cell injury (*i.e.* KIM-1 expression) (Fig. 3d-e). NKp46<sup>+</sup> ILC were the main CSF2-expressing population in glomerular areas following poly(I:C) stimulation of *Csf2*-tdTomato reporter mice and NKp46<sup>+</sup> CSF2<sup>+</sup> ILC were associated with macrophages. We confirmed this association in nephritic NZB/W F1 mice (Fig. 3f-g). Thus, NKp46 signaling controls CSF2 production by NKp46<sup>+</sup> tILC associated with macrophages and NKp46<sup>+</sup> tILC-derived CSF2 is required for autoimmune organ damage.

## NKp46 controls monocyte-derived macrophages

We asked whether blocking of NKp46 may regulate disease-associated macrophage population dynamics in lupus nephritis. Tissue macrophages were CD11blow and MHCIIhigh in control mice, but CD11bhigh in nephritis (Fig. 4a). The latter included a MHCIIhigh and a MHCIIlow/- subset. NKp46 blocking did not reinstate the homeostatic phenotype (CD11blow MHCIIhigh), but it substantially diminished the numbers of disease-associated, periglomerular, and peritubular macrophages (Fig. 4a-b). In particular, anti-NKp46 affected the MHCIIlow disease-associated macrophage subset. Numbers of vessel-associated (CD45*i.v.*+) monocytes and accumulation of CD45*i.v.*+ cells within the glomeruli were not reduced by NKp46 blockade (Extended Data Fig. 7a-d). Similar effects on disease-associated macrophages were observed with CSF2 blocking (Fig. 4c). Thus, CSF2-producing NKp46+ tILC are associated with macrophages around glomeruli and NKp46 activation controls the population expansion of disease-associated macrophages via CSF2.

Transcriptional analysis of immune cells subclustered from the whole kidney dataset showed that tissue-resident macrophages (TR-M $\Phi$ ) were significantly under-represented in nephritic kidneys, while three lupus nephritis-associated M $\Phi$  clusters were over-represented (clusters LN-M $\Phi$ 1, LN-M $\Phi$ 2, LN-M $\Phi$ 3); this was reversed by depletion of NKp46<sup>+</sup> tILC (Fig. 4d, Extended Data Fig. 7e). Unbiased analysis of differentially co-regulated genes across conditions and monocyte/macrophage clusters identified three modules (Extended Data Fig. 7f): Module 1 genes were related to phagocytosis (Cd36, Fcer1g), migration (Ccr2), production of reactive oxygen species (Cybb), and alternative activation (Chil1). Module 2 genes contained homeostatic macrophage markers, such as Mafb and C1q, but also Maf, Mrc1, Apoe and Trem2. TREM2 is a transmembrane receptor binding lipoproteins, phospholipids, and apoptotic cells, promoting phagocytosis, removal of apoptotic cells and macrophage population expansion<sup>29,30</sup>. Module 3 was dominated by ribosomal genes.

GO term analysis for biological processes and analysis of genes differentially expressed across immune cells confirmed that macrophages were enriched in antigen processing and presentation, phagocytosis and complement regulation, 'phospholipid binding' and 'lipoprotein particle binding' (Extended Data Fig. 7g). They expressed transcripts associated with phagocytosis and lysosomal processing (*Trem2*, *Mrc1*, *Lgmn*), cholesterol metabolism (*Apoe*, *Abca1*) and leukocyte recruitment (*Vcam1*, *Ccr2*, *Vcam1*) (Extended Data Fig. 7h). LN-MΦ3 were enriched in genes related to cell cycle and proliferation (*Ccnb1*, *Ccnb2*, *Cdk1*) and in *Cfp*, encoding the NKp46 ligand properdin (Extended Data Fig. 7i). Monocytes were enriched in pathways related to reactive oxygen species, Fc receptor-mediated phagocytosis and NF-κB signaling. Analysis of a renal leukocyte dataset from human lupus nephritis patients<sup>28</sup> confirmed that *TREM2* expression faithfully marks LN-MΦ in lupus nephritis across species (Extended Data Fig. 7j).

Strikingly, Trem2 expression correlated with the expression of genes that were enriched in LN-MΦs, including Mrc1, Ctsl, Lgmn, Abca1, Vcam1 and Ccl12. In contrast, upregulation of Trem2 negatively correlated with the expression levels of pro-inflammatory transcripts, such as Nfkb and *Irf5* (Fig. 4e). Thus, *Trem2* upregulation is linked to a LN-MΦ transcriptional program promoting uptake and processing of apoptotic cells and negatively correlates with pro-inflammatory transcripts. Since Trem2 positively correlated with Mrc1 transcripts (encoding the mannose receptor C-type 1 or CD206, a marker of anti-inflammatory macrophages), we used CD206 as a surrogate marker to explore the location of Trem2hi macrophages, using multiplexed tissue imaging. CD206<sup>+</sup> macrophages were in periglomerular areas and associated with activated tubular epithelial cells (Extended Data Fig. 7k), suggesting a role of Trem2hi macrophages in mounting a response to tissue damage. Although macrophages at homeostasis expressed very low levels of Csf2rb and Trem2, both were highly expressed by disease-associated macrophages during nephritis; this was abrogated by NKp46 blocking (Fig. 4f, Extended Data Fig. 8a-b). Analysis of differentially expressed genes by  $Csf2rb^+vs$ .  $Csf2rb^-$  macrophages revealed that  $Csf2rb^+$  macrophages expressed a pro-inflammatory program reminiscent of monocytes (i.e. C3, Myd88, Nr4a1, Ikbke, Itgb7, Cebpb, Plac8, Lyz2, Itga4, Cxcl2, S100a4, S100a6), whereas they expressed lower levels of genes expressed by homeostatic macrophages (*Hexb*, *Clqa*) (Fig. 4g, Supplementary Table 4). We next analyzed the two major phenotypic subsets of disease-associated macrophages (Fig. 4a) by bulk RNA-seq. Compared to MHCIIhi CD11bhi macrophages, MHCIIlow macrophages expressed lower levels of disease-associated macrophage signature genes (e.g., Trem2, Mrc1, Clga, Mertk, Axl), but higher levels of monocyte-related genes (e.g., Cxcr4, Nr4a1, Plac8, S100a4, S100a6) and Spp1, encoding Osteopontin, a profibrotic molecule<sup>31,32</sup> (Extended Data Fig.

306

307

308

309

310

311

312

313

314

315

316

317

318

319

320

321

322

323

324

325

326

327

9c). Collectively, the data reveal a spectrum of disease-associated macrophage programs: at the one end of the spectrum were  $Csf2rb^{hi}$  cells with a monocyte-related, pro-inflammatory and profibrotic program and at the other end  $Trem2^{hi}$  macrophages with an anti-inflammatory, phagocytic, lipid-processing profile. CSF2-producing NKp46<sup>+</sup> ILC regulated the population expansion of all disease-associated macrophages, and particularly of the  $Csf2rb^{hi}$  MHCII<sup>low</sup> subset.

Do NKp46-regulated macrophages derive from blood monocytes? RNA velocity analysis predicted no contribution of Ly6C<sup>low</sup> monocytes (cluster Mo2) to tissue macrophage clusters (Fig. 4h). However, it predicted that *Ccr2*<sup>+</sup> macrophages, with possible contribution of Ly6C<sup>hi</sup> monocytes (cluster Mo1) may transition to LN-MΦs, while TR-MΦ may be a second source of LN-MΦs. To address if longer-lived kidney-resident macrophages or bone marrow-derived monocytes sustain the pool of disease-associated macrophages, we employed *Cx3cr1*<sup>CreERT2</sup>; *R26R*<sup>tdTomato</sup> mice treated with tamoxifen, followed by a chase period of 8 weeks, followed by no treatment vs. poly(I:C). In control mice, most CD45*i.v.* macrophages were tdTomato<sup>+</sup>, *i.e.* kidney-resident macrophages (Extended Data Fig. 9a-b). Poly(I:C) induced a 'replacement' of tdTomato<sup>+</sup> by tdTomato<sup>-</sup> macrophages. This was reversed by CSF2 blocking. Thus, disease-associated macrophages receive substantial contributions from blood monocytes and the population size of monocyte-derived macrophages is controlled by CSF2.

To explore the contribution of monocyte-derived macrophages in nephritis, we labelled circulating cells with CD45.2 antibodies coupled to two different fluorochromes injected intravenously 5 min and 12 h before analysis<sup>33</sup>. Myeloid cells were thus divided into 4 categories: '5min vessel-associated', '12 h vessel-associated', 'recruited within 12 h tissue cells', and 'tissue cells', the latter representing tissue-resident cells or recruited 12h prior to analysis (Extended Data Fig. 9c). Ly6Chi monocytes were enriched in the gate '5 min vessel-associated' but were absent

from tissues (Extended Data Fig. 9d). In contrast, Ly6C<sup>lo</sup> CD43<sup>+</sup> monocytes were enriched in the '12 h vessel-associated' gate. MHC II<sup>low</sup> macrophages were particularly enriched in the gate 'recruited within 12h tissue cells' (Extended Data Fig. 9e). Collectively, RNA velocity analysis, fate labelling of CX3CR1<sup>+</sup> cells and an *i.v.* labelling approach, support that NKp46<sup>+</sup> ILC control the population expansion of monocyte-derived macrophages via CSF2.

## TREM2 regulates monocyte-derived macrophages

To explore whether disease-associated macrophage depletion regulate tissue damage and NKp46-dependent glomerular fibrosis (Fig. 1m), we blocked CSF1R signaling (Fig. 5a-b, Extended Data Fig. 9f-g). Complete depletion of macrophages by CSF1R blocking suppressed periglomerular fibrosis. CD45*i.v.*<sup>+</sup> monocyte numbers were not affected. Thus, macrophages are required for periglomerular fibrosis, a hallmark of severe lupus nephritis.

To explore whether TREM2, expressed specifically by disease-associated macrophages (Fig. 5c), regulates disease progression, we generated B6.*Sle1Yaa*; *Trem2*-/- mice. *Trem2* deficiency did not affect the numbers of MHCII<sup>hi</sup> disease-associated macrophages, nor vessel-associated Ly6C<sup>low</sup> and Ly6C<sup>hi</sup> monocytes (Extended Data Fig. 9h-i). In contrast, B6.*Sle1Yaa*; *Trem2*-/- mice had significantly higher numbers of MHCII<sup>low</sup> macrophages, expressing the monocyte marker CD43 (Fig. 5d). *Trem2* deficiency resulted in increased levels of periglomerular smooth muscle actin and distorted periglomerular capillary architecture (Fig. 5f). TREM2 may thus accelerate monocytederived macrophage differentiation towards an anti-inflammatory state.

#### Discussion

Amplifiers of autoimmune tissue damage are largely elusive. Our data uncover that NKp46 signaling regulates interactions of ILC1, disease-associated macrophages, and kidney parenchymal cells, resulting in amplification of the inflammatory cascades that cause organ damage without affecting autoimmunity (Extended Data Fig. 10). ILC3-derived CSF2 has been linked to monocyte-derived macrophage programs in the intestine<sup>34-36</sup>. In lupus nephritis, NKp46 signaling in ILC1 instructs an immunoregulatory ILC3-like program controlling the population expansion of disease-promoting monocyte-derived macrophages via CSF2-CSF2R interactions. Disruption of this cascade ameliorated kidney disease in SLE supporting that NKp46-driven activation of ILC1 is an essential amplifier of nephritis severity. Our data do not exclude an additional role of vessel-associated cytotoxic NK cells in disease progression, but our findings that they were not depleted by extended anti-AGM1 treatment and had rather low cytotoxic activity when compared to splenic NK cells, do not support a primary role of NK cells. An open question remains how the NKp46 receptor is triggered during lupus nephritis. A potential ligand is properdin, a serum glycoprotein that activates the alternative complement pathway and that can bind to apoptotic cells<sup>37</sup>. We found that properdin is expressed by disease-associated mononuclear phagocytes in nephritic mice, suggesting a bi-directional crosstalk between NKp46<sup>+</sup> ILC and monocyte-derived macrophages. The localized expression of CSF2 by a limited number of NKp46<sup>+</sup> ILC in the kidney parenchyma suggests spatially targeted interactions of ILC1 with CSF2R-expressing monocyte-derived macrophages. Monocyte-derived macrophages in a second step upregulate TREM2, which suppresses pro-inflammatory macrophage programs and promotes epithelial cell repair. The latter may be a broader function of TREM2 in chronic kidney diseases<sup>38</sup>. These findings provide a deeper understanding of the molecular determinants of host susceptibility

374

375

376

377

378

379

380

381

382

383

384

385

386

387

388

389

390

391

392

393

394

396 to autoimmune organ damage, with broad implications for the immunotherapy of chronic

inflammatory diseases.

398399

#### 400 REFERENCES

- 401 1 Tsokos, G. C. *et al.* The immunoregulatory roles of non-haematopoietic cells in the kidney. 402 *Nat Rev Nephrol* **20**, 206-217 (2024). <a href="https://doi.org:10.1038/s41581-023-00786-x">https://doi.org:10.1038/s41581-023-00786-x</a>
- 403 2 Yossef, R. *et al.* Targeting natural killer cell reactivity by employing antibody to NKp46: implications for type 1 diabetes. *PLoS One* **10**, e0118936 (2015). https://doi.org:10.1371/journal.pone.0118936
- 406 3 Vivier, E. *et al.* Innate Lymphoid Cells: 10 Years On. *Cell* **174**, 1054-1066 (2018). 407 <a href="https://doi.org:10.1016/j.cell.2018.07.017">https://doi.org:10.1016/j.cell.2018.07.017</a>
- 408 4 Triantafyllopoulou, A. *et al.* Proliferative lesions and metalloproteinase activity in murine lupus nephritis mediated by type I interferons and macrophages. *Proc Natl Acad Sci U S A* **107**, 3012-3017 (2010). <a href="https://doi.org:10.1073/pnas.0914902107">https://doi.org:10.1073/pnas.0914902107</a>
- Klose, C. S. N. *et al.* Differentiation of type 1 ILCs from a common progenitor to all helper-like innate lymphoid cell lineages. *Cell* **157**, 340-356 (2014). <a href="https://doi.org:10.1016/j.cell.2014.03.030">https://doi.org:10.1016/j.cell.2014.03.030</a>
- Kasai, M. *et al.* In vivo effect of anti-asialo GM1 antibody on natural killer activity. *Nature* **291**, 334-335 (1981). <a href="https://doi.org:10.1038/291334a0">https://doi.org:10.1038/291334a0</a>
- Vonarbourg, C. *et al.* Regulated expression of nuclear receptor RORγt confers distinct functional fates to NK cell receptor-expressing RORγt(+) innate lymphocytes. *Immunity* 33, 736-751 (2010). <a href="https://doi.org:10.1016/j.immuni.2010.10.017">https://doi.org:10.1016/j.immuni.2010.10.017</a>
- 419 8 Nagata, M. Podocyte injury and its consequences. *Kidney Int* **89**, 1221-1230 (2016). 420 <a href="https://doi.org:10.1016/j.kint.2016.01.012">https://doi.org:10.1016/j.kint.2016.01.012</a>
- 421 9 Kuppe, C. *et al.* Novel parietal epithelial cell subpopulations contribute to focal segmental description glomerulosclerosis and glomerular tip lesions. *Kidney Int* **96**, 80-93 (2019). https://doi.org:10.1016/j.kint.2019.01.037
- Eymael, J. *et al.* CD44 is required for the pathogenesis of experimental crescentic glomerulonephritis and collapsing focal segmental glomerulosclerosis. *Kidney Int* **93**, 626-426 642 (2018). <a href="https://doi.org:10.1016/j.kint.2017.09.020">https://doi.org:10.1016/j.kint.2017.09.020</a>
- Lazareth, H. *et al.* The tetraspanin CD9 controls migration and proliferation of parietal epithelial cells and glomerular disease progression. *Nat Commun* **10**, 3303 (2019). https://doi.org:10.1038/s41467-019-11013-2
- Dumas, S. J. *et al.* Phenotypic diversity and metabolic specialization of renal endothelial cells. *Nat Rev Nephrol* **17**, 441-464 (2021). https://doi.org:10.1038/s41581-021-00411-9
- Hong, Q. *et al.* LRG1 Promotes Diabetic Kidney Disease Progression by Enhancing TGFbeta-Induced Angiogenesis. *J Am Soc Nephrol* **30**, 546-562 (2019). https://doi.org:10.1681/ASN.2018060599
- 435 14 Li, X. et al. Overexpression of SerpinE2/protease nexin-1 Contribute to Pathological
  436 Cardiac Fibrosis via increasing Collagen Deposition. Sci Rep 6, 37635 (2016).
  437 https://doi.org:10.1038/srep37635

- Conway, D. E. *et al.* Endothelial metallothionein expression and intracellular free zinc levels are regulated by shear stress. *Am J Physiol Cell Physiol* **299**, C1461-1467 (2010). <a href="https://doi.org/10.1152/ajpcell.00570.2009">https://doi.org/10.1152/ajpcell.00570.2009</a>
- 441 16 Tian, X. Y., Ma, S., Tse, G., Wong, W. T. & Huang, Y. Uncoupling Protein 2 in 442 Cardiovascular Health and Disease. Front Physiol 9, 1060 (2018). 443 https://doi.org:10.3389/fphys.2018.01060
- Weiss, N., Zhang, Y. Y., Heydrick, S., Bierl, C. & Loscalzo, J. Overexpression of cellular glutathione peroxidase rescues homocyst(e)ine-induced endothelial dysfunction. *Proc Natl Acad Sci U S A* 98, 12503-12508 (2001). <a href="https://doi.org:10.1073/pnas.231428998">https://doi.org:10.1073/pnas.231428998</a>
- Saxena, S. & Zou, L. Hallmarks of DNA replication stress. *Mol Cell* 82, 2298-2314 (2022).
   <a href="https://doi.org:10.1016/j.molcel.2022.05.004">https://doi.org:10.1016/j.molcel.2022.05.004</a>
- 449 19 Liu, J. et al. Tcf1 Sustains the Expression of Multiple Regulators in Promoting Early
  450 Natural Killer Cell Development. Front Immunol 12, 791220 (2021).
  451 https://doi.org:10.3389/fimmu.2021.791220
- Zhang, Q. *et al.* Blockade of the checkpoint receptor TIGIT prevents NK cell exhaustion and elicits potent anti-tumor immunity. *Nat Immunol* **19**, 723-732 (2018). <a href="https://doi.org:10.1038/s41590-018-0132-0">https://doi.org:10.1038/s41590-018-0132-0</a>
- Wang, W. *et al.* Tumor-released Galectin-3, a soluble inhibitory ligand of human NKp30, plays an important role in tumor escape from NK cell attack. *J Biol Chem* **289**, 33311-33319 (2014). <a href="https://doi.org/10.1074/jbc.M114.603464">https://doi.org/10.1074/jbc.M114.603464</a>
- 458 22 Merino, A. M., Kim, H., Miller, J. S. & Cichocki, F. Unraveling exhaustion in adaptive 459 and conventional NK cells. *J Leukoc Biol* **108**, 1361-1368 (2020). 460 <a href="https://doi.org/10.1002/jlb.4mr0620-091r">https://doi.org/10.1002/jlb.4mr0620-091r</a>
- Friedrich, C. *et al.* Effector differentiation downstream of lineage commitment in ILC1s is driven by Hobit across tissues. *Nat Immunol* **22**, 1256-1267 (2021). <a href="https://doi.org/10.1038/s41590-021-01013-0">https://doi.org/10.1038/s41590-021-01013-0</a>
- 464 24 Yomogida, K. *et al.* Hobit confers tissue-dependent programs to type 1 innate lymphoid cells. *Proc Natl Acad Sci U S A* **118** (2021). <a href="https://doi.org:10.1073/pnas.2117965118">https://doi.org:10.1073/pnas.2117965118</a>
- 466 25 Yeh, J. H., Sidhu, S. S. & Chan, A. C. Regulation of a late phase of T cell polarity and effector functions by Crtam. *Cell* 132, 846-859 (2008). <a href="https://doi.org/10.1016/j.cell.2008.01.013">https://doi.org/10.1016/j.cell.2008.01.013</a>
- Cortez, V. S. *et al.* CRTAM controls residency of gut CD4+CD8+ T cells in the steady state and maintenance of gut CD4+ Th17 during parasitic infection. *J Exp Med* **211**, 623-633 (2014). <a href="https://doi.org:10.1084/jem.20130904">https://doi.org:10.1084/jem.20130904</a>
- Yokogawa, M. *et al.* Epicutaneous application of toll-like receptor 7 agonists leads to systemic autoimmunity in wild-type mice: a new model of systemic Lupus erythematosus. *Arthritis Rheumatol* **66**, 694-706 (2014). <a href="https://doi.org:10.1002/art.38298">https://doi.org:10.1002/art.38298</a>
- 475 28 Arazi, A. *et al.* The immune cell landscape in kidneys of patients with lupus nephritis. *Nat Immunol* **20**, 902-914 (2019). <a href="https://doi.org:10.1038/s41590-019-0398-x">https://doi.org:10.1038/s41590-019-0398-x</a>
- Deczkowska, A., Weiner, A. & Amit, I. The Physiology, Pathology, and Potential Therapeutic Applications of the TREM2 Signaling Pathway. *Cell* **181**, 1207-1217 (2020). https://doi.org:10.1016/j.cell.2020.05.003
- 480 30 Colonna, M. The biology of TREM receptors. *Nat Rev Immunol*, 1-15 (2023). 481 <a href="https://doi.org:10.1038/s41577-023-00837-1">https://doi.org:10.1038/s41577-023-00837-1</a>

- Hoeft, K. *et al.* Platelet-instructed SPP1(+) macrophages drive myofibroblast activation in fibrosis in a CXCL4-dependent manner. *Cell Rep* **42**, 112131 (2023). <a href="https://doi.org/10.1016/j.celrep.2023.112131">https://doi.org/10.1016/j.celrep.2023.112131</a>
- 485 32 Morse, C. *et al.* Proliferating SPP1/MERTK-expressing macrophages in idiopathic pulmonary fibrosis. *Eur Respir J* **54** (2019). <a href="https://doi.org:10.1183/13993003.02441-2018">https://doi.org:10.1183/13993003.02441-2018</a>
- Kirschenbaum, D. *et al.* Time-resolved single-cell transcriptomics defines immune trajectories in glioblastoma. *Cell* **187**, 149-165.e123 (2024). <a href="https://doi.org:10.1016/j.cell.2023.11.032">https://doi.org:10.1016/j.cell.2023.11.032</a>
- Chiaranunt, P. *et al.* Microbial energy metabolism fuels an intestinal macrophage niche in solitary isolated lymphoid tissues through purinergic signaling. *Sci Immunol* **8**, eabq4573 (2023). https://doi.org:10.1126/sciimmunol.abq4573
- 493 35 Mortha, A. *et al.* Microbiota-dependent crosstalk between macrophages and ILC3 494 promotes intestinal homeostasis. *Science* **343**, 1249288 (2014). 495 <a href="https://doi.org:10.1126/science.1249288">https://doi.org:10.1126/science.1249288</a>
- 496 36 Castro-Dopico, T. *et al.* GM-CSF Calibrates Macrophage Defense and Wound Healing 497 Programs during Intestinal Infection and Inflammation. *Cell Rep* **32**, 107857 (2020). 498 <a href="https://doi.org/10.1016/j.celrep.2020.107857">https://doi.org/10.1016/j.celrep.2020.107857</a>
- Narni-Mancinelli, E. *et al.* Complement factor P is a ligand for the natural killer cell-activating receptor NKp46. *Sci Immunol* **2** (2017). <a href="https://doi.org:10.1126/sciimmunol.aam9628">https://doi.org:10.1126/sciimmunol.aam9628</a>
- 502 38 Subramanian, A. *et al.* Protective role for kidney TREM2(high) macrophages in obesity-503 and diabetes-induced kidney injury. *Cell Rep* **43**, 114253 (2024). 504 <a href="https://doi.org/10.1016/j.celrep.2024.114253">https://doi.org/10.1016/j.celrep.2024.114253</a>

# Figure legends

505506

507

508

## Figure 1. NKp46<sup>+</sup> ILC control autoimmune organ damage

- a, Flow cytometry plots and quantification of kidney NKp46<sup>+</sup> ILC subsets (left to right, mice per
- group: n = 5, 6, 6). Representative of 2 independent experiments. **b-e**, Quantification of serum
- BUN, anti-dsDNA antibody titers and *Haver1* expression in renal cortex from NZB/W F1 mice
- 513 (mice per group: n = 9, 12, 11 for **b-c**; n = 18, 12, 8 for **d**-BUN; n = 4, 6, 4 for **d**-Haver1; n = 4,
- 514 6, 6 for e). Pooled from (b, c, d-BUN) or representative of (d-Haver1, e) 2 independent
- experiments. f, UMAP plot of 74,850 whole kidney cells (n = 3 mice per group). PT, proximal
- 516 tubular cell; STR, stromal cell; NP, nephron progenitors; IMU, immune cell; LOH, loop of Henle;

EC, endothelial cell; DCT, distal convoluted tubule; PEC/Pod, parietal epithelial cell/podocyte; IC, intercalated cell; CD, collecting duct. g, UMAP plot of 1294 PEC/Podocytes. iPEC, intermediate PEC; LN-iPEC, LN-associated iPEC; fPEC, flat PEC; LN-fPEC, LN-associated fPEC; Pod, podocyte. h, Distribution of each experimental group on the UMAP plot. i, Feature plots of Nphs2, Ccl2, and Acta2 in the indicated groups. j, Pseudotime heatmap depicting expression of significant marker genes corresponding to three expression modules spanning the transition from PEC to Pod. Color scale indicates scaled marker gene expression across pseudotime. Representative genes included in each module are shown. k, Matrix plot indicating log2-transformed row scaled expression of exemplar genes selected from each module shown in j. **l-m**, α–SMA (light teal) and DAPI (grey) or CD44 (yellow) and F4/80 (dark purple) immunofluorescence (IF) images of kidney cortex and quantification of periglomerular  $\alpha$ -SMA<sup>+</sup> and CD44<sup>+</sup> area per visual field (visual fields: n = 10, 14, 23 pooled from 3, 4, 3 mice per group for I, and n = 5, 18, 11 pooled from 2 mice per group for m), n, CD31 (grey), F4/80 (vermilion) and KIM-1 (light teal) IF images of kidney cortex and quantification of KIM-1<sup>+</sup> area (n = 12 visual fields pooled from 4 mice per group). o, Haver 1 expression in renal cortex from imiquimod-treated BALB/c mice (n = 5, 6, 7, 8 mice per group). **p,** Quantification of serum BUN (n = 5, 3, 7, 8 mice per group). One-way ANOVA followed by Tukey's test (a-e, p-q) or Kruskal-Wallis test followed by Dunn's test (**l-n**). Bars show mean  $\pm$  SD.

535

536

537

538

539

534

517

518

519

520

521

522

523

524

525

526

527

528

529

530

531

532

533

## Figure 2. An NKp46-instructed immunoregulatory program.

**a**, UMAP plot of 17,766 single-cell transcriptomes of kidney tissue NKp46<sup>+</sup> ILC, colored by cell annotation. tILC, tissue 'helper' innate lymphoid cell; tNK, tissue natural killer cell. **b**, Feature plots of selected marker genes (*Eomes, Klra8, Zfp683, Il7r, Il2ra, Csf2*, and *Csf1*), split into young

and nephritis-1 conditions. **c**, Volcano plot showing differentially expressed genes (DEG) of  $Tnfrsf9^+$  tILC from young vs. nephritis-1. **d**, Violin plots showing levels of expression of an NKp46 activation<sup>37</sup> signature across the kidney tissue NKp46<sup>+</sup> ILC clusters. **e**, Composition of tissue NKp46<sup>+</sup> tILC split into the indicated conditions. The bars show mean  $\pm$  SD.

544

545

546

547

548

549

550

551

552

553

554

555

556

557

558

559

560

561

562

540

541

542

543

## Figure 3. NKp46 signaling in NKp46<sup>+</sup> ILC amplifies renal injury via CSF2.

a, Representative flow cytometry plots of kidney NK1.1<sup>+</sup> ILC stimulated with plate-bound NKp46 or isotype, analyzed for CD49b and CD45. Indicated subsets were analyzed for CSF2. Right: Percent of CSF2<sup>+</sup> cells among CD49b<sup>-</sup> NKp46<sup>+</sup> ILC per condition. **b**, Dot plot showing the expression levels of Csf2 across tissue (CD45.2i.v.-) NKp46<sup>+</sup> ILC clusters, split into isotype (nephritis-2) and anti-NKp46 treated conditions. Dot size indicates percentage of expressing cells (% Exp.), and color scale shows average expression level of log normalized counts (Avg Exp.) c, Quantitative PCR of Csf2 in kidney cortex; relative to expression of Gapdh. (left to right: n = 3, 3, 4, 6 top; n = 4, 6, 7, 8 mice per group bottom). **d**, Quantification of urine Albumin/Creatinine Ratio and serum BUN (n = 3, 6, 6 mice per group). e, CD31 (grey), F4/80 (vermilion) and KIM-1 (light teal) IF of kidney cortex and quantification of KIM-1 area per visual field (n = 9, 9, 12 visual fields pooled from 3, 3, 4 mice per group). f, Tdtomato (vermilion), NKp46 (light teal) and DAPI (grey) IF images of kidney cortex and percentage of NKp46 + and NKp46 - Csf2-TdTomato + cells per visual field (n = 23, 49 visual fields pooled from 3 mice per group). g, Left: F4/80 (light teal), TdTomato (vermilion), and NKp46 (grey) IF images of kidney cortex and quantification of Csf2<sup>+</sup> NKp46<sup>+</sup> ILC associated with macrophages (M $\Phi$ ) per 10 visual fields (n = 3 mice per group). Right: NKp46 (grey), F4/80 (light teal), and EOMES (light teal) and DAPI (dark blue) IF images of kidney cortex, representative of 3 mice. Two-tailed paired t-Test (a); one-way ANOVA followed

by Tukey's test (c, e); Kruskal-Wallis test followed by Dunn's test (f); two-tailed unpaired t-Test (g, h). The bars show mean  $\pm$  SD.

565

566

567

568

569

570

571

572

573

574

575

576

577

578

579

580

581

563

564

## Figure 4. NKp46 signaling controls disease-associated macrophages

a, c, Representative flow cytometry plots of kidney M $\Phi$ , analyzed for MHC II and CD11b and quantification of M $\Phi$  subsets (left to right: n = 4, 6, 4 mice per group for **a** and n = 4, 6, 6 for **c**), representative of 2 independent experiments. b, CD31 (grey), F4/80 (dark purple) IF images of kidney cortex, representative of 4 mice per group. White arrows point to periglomerular and yellow arrows to peritubular areas. **d**, UMAP plot of 4,769 immune cells, TR-M $\Phi$ , tissue resident M $\Phi$ ; LN-MΦ, lupus nephritis (LN)-associated MΦ; Ccr2<sup>+</sup> MΦ, MΦ enriched in Ccr2 transcripts; Mo, Monocyte; PMN, polymorphonuclear neutrophils; cDC, conventional dendritic cell; PC, plasma cells; T, T cell; UNO, unidentified cells. Bottom: Distribution of each experimental group on the UMAP plot. e, Heatmap of significantly coregulating genes (adjusted p-value < 0.05) in immune cells. Color scale indicates Spearman's rank correlation coefficient (r). Top bar plots show Spearman's rank correlation coefficient to *Trem2*. f, Violin plots showing levels of expression of Trem2 and Csf2rb in M $\Phi$  clusters split into the indicated conditions. **g**, Volcano plot showing DEG by  $Csf2rb^+$  vs  $Csf2rb^-$  macrophages (pseudobulk analysis of M $\Phi$  clusters 2,18, 27, shown in Extended Data Fig. 8a). h, RNA velocity analysis of kidney immune cell subpopulations from nephritic kidneys. One-way ANOVA followed by Tukey's test (a, c). The bars show mean  $\pm$  SD.

582

583

584

585

## Fig. 5 TREM2 regulates monocyte-derived macrophages.

**a-b**, Experimental set up in Extended Data Fig. 9f. **a**, CD31 (grey), F4/80 (dark purple) and smooth muscle actin (α-SMA, light teal) IF images of kidney cortex and quantification of periglomerular

 $\alpha$ -SMA<sup>+</sup> area per visual field. Each Dot is average value per mouse. (n=6 mice per group pooled from 3 independent experiments). **b**, Representative flow cytometry plots of kidney M $\Phi$ , analyzed for CD11b and MHC2 and quantification of the indicated M $\Phi$  subsets (n=4, 6, 6 mice per group). **c**, Dot plot showing the expression levels of *Trem2* across whole kidney cell populations (left), or across immune cell clusters (right). Dot size indicates percentage of expressing cells (% Exp.) and color scale shows average expression level of log-normalized counts (Avg Exp.). **d**, Representative flow cytometry plots of kidney M $\Phi$  stained for MHC2 and CD11b (top) or MHC2 and CD43 (bottom) and quantification of the indicated M $\Phi$  subsets (n=3, 12, 7 mice per group). **e**,  $\alpha$ -SMA (light teal), F4/80 (dark purple) and CD31 (grey) IF images of kidney cortex and quantification of periglomerular  $\alpha$ -SMA<sup>+</sup> area per visual field. Each dot is average value per mouse (n=6, 10, 8 mice per group). **b**, **d**, one-way ANOVA followed by Tukey's test. **a**, **e**, Kruskal-Wallis test followed by Dunn's test. The bars show mean  $\pm$  SD.

#### Methods

Mice

NZB/W F1, NZB, NZW, BALB/c mice were purchased from Jackson Laboratory or bred in house. Eomes<sup>fl/fl 39</sup>, Gata3<sup>fl/fl 40</sup>, *Ncr1*-Cre<sup>Tg 41</sup>, *Rorc(\gamma)*-Cre<sup>Tg 42</sup>, *Rosa26*-LSL-YFP<sup>43</sup>, *Eomes*<sup>Gfp/+ 44</sup>, all on the C57BL/6 background, were bred locally. B6.*Sle1.Yaa* mice<sup>45,46</sup> were purchased from Jackson Laboratory or imported from the University of Oxford and crossed locally to *Trem2*-/- mice<sup>47</sup>. *Ncr1*<sup>gfp/gfp</sup> mice on a BALB/c background<sup>48</sup> were imported from the University of Rijeka and bred locally. *Csf2*-tdTomato reporter mice<sup>49</sup> mice were imported from the University of Zurich and bred locally. All mice were kept in the FEM animal facility of the Charité University under Standard Pathogen-Free conditions. All animal experiments were approved and were in accordance with the

guidelines of the local animal care and use committees (Landesamt für Gesundheit und Soziales, Berlin).

611

612

613

614

615

616

617

618

619

620

621

622

623

624

625

626

627

628

629

630

609

610

## poly (I:C)-induced lupus nephritis and in vivo treatments

The poly (I:C)-induced lupus nephritis model has been previously described<sup>4</sup>. Briefly, 19-weekold female mice were treated i.p. with 200µg poly (I:C) (Invivogen, San Diego, CA) in sterile endotoxin-free water three times per week for 4 weeks and analysed 2 weeks after the last poly (I:C) injection. Indicated groups of mice were treated i.p. with anti-NKp46 (mNCR1.15, IgG1k, 150µg per injection, provided by Stipan Jonjic, University of Rijeka, Center of Proteomics), anti-CSF1R (clone AFS98, rat IgG2ak, BioXCell Catalog #BE0213, 300µg per injection,), anti-CSF2 (clone MP1-22E9, rat IgG2ak, BioXCell Catalog #BE0259, 300µg per injection with a loading dose of 500µg) or isotype control of the same quantity (IgG1k, clone MOPC-21, BioXCell Catalog #BE0083 and IgG2a clone 2A3, BioXCell Catalog #BE0089). Anti-IFNAR (clone MAR15A3, BioXCell Catalog #BE024, 250µg per injection) and anti-AGM1 antibodies (FUJIFILM Wako Chemicals 20µl solution) were injected twice a week for 6 weeks. Where indicated in the figures, rabbit polyclonal IgG (BioXCell Catalog #BE0095, 200 µg per injection) was used as control to anti-AGM1. Anti-CSF1R, and anti-NKp46 or isotype control were injected every other day for 2 weeks following the 4-week poly (I:C)-treatment. Anti-CSF2 was either injected every other day for 2 weeks or daily for 1 week, following poly (I:C) treatment. Cx3cr1<sup>CreERT2</sup>; R26R<sup>tdTomato</sup> mice were injected with two tamoxifen injections as previously described<sup>50</sup>. poly (I:C) and anti-CSF2 were injected 8 weeks later i.p. for two weeks. Where indicated, mice were injected with anti-CD45.2 antibodies *i.v.* before analysis.

The monoclonal anti-NKp46 blocking antibody (Clone mNCR1.15, isotype IgG1k, Antigen/Immunogen: mNCR1 ectodomain fused to hIgG1 Fc fragment) has been extensively described<sup>2</sup>. mNCR1.15 was produced by Stipan Jonjic, University of Rijeka, Center for Proteomics. Briefly, hybridoma cells were cultured in RPMI 1640 media, antibodies were purified from the serum-free medium using an AKTA Pure system equipped with prepacked protein G columns with one column dedicated to each clone. For every lot, a battery of tests was conducted, including one functional test per clone.

The imiquimod-induced lupus nephritis model has been previously described<sup>27</sup>. Topical Imiquimod (ALDARA® 5 % cream, Viatris Healthcare GbmH, 25mg creme containing 1.25mg Imiquimod per application) was applied every other day on the dorsal surface of the right ear for 5-7 weeks. All mice were analysed within 7 days after the onset of proteinuria.

#### Immunofluorescence on tissue sections and confocal microscopy

Kidneys were fixed in PLP containing PFA overnight at 4°C. The tissue was washed and incubated again overnight in 30% sucrose in phosphate buffer and subsequently frozen in O.C.T. Tissue Tek (Sakura) and stored at -80°C. For analysis, 10-20 μm sections were cut using the cryotomes Nx70 or HM560 (ThermoFisher). Sections were dried, rehydrated, and blocked for 1 h with 1% bovine serum albumin (BSA) and 10% donkey serum (Jackson Immunoresearch, 017-000-121) and 20 min with Fc-block FcgRI/III (Invitrogen) and FcgRIV (Biolegend). Unlabelled primary antibodies against NKp46 (R&D Systems, polyclonal), EOMES (R&D Systems, clone 1219A), TIM1/KIM1/HAVCR (R&D Systems, polyclonal) and RFP/ DsRed/ TdTomato (Rockland, polyclonal) were diluted in PBS with 1% BSA and 0.1% Triton X-100 in PBS and sections were

incubated overnight at 4°C. Sections were incubated with secondary antibodies, including donkey anti-goat-AF488, donkey anti-goat-AF594, donkey anti-goat-AF647, goat anti-rabbit-AF546, goat anti-rabbit-AF594 (ThermoFisher Scientific), followed by directly conjugated antibodies CD31-AF594 (Biolegend, clone MEC13.3) or CD31-AF647 (BioLegend, clone 390), F4/80-AF488 and F4/80-e660 (Invitrogen, clone BM8), α-Smooth Muscle Actin-AF488 (Cell Signaling, clone 1A4) CD11b-AF488 (eBioscience, clone M1/70) and CD44-AF594 (DRFZ, clone IM7), sequentially for 1-2h each at room temperature. For nuclear staining, sections were stained with 1μg per ml DAPI (Thermofisher) in PBS and the slides were mounted using Fluorescence Mounting Medium (Agilent, S302380-2). The slides were imaged on a Laser-Scanning-Microscope (LSM 880, Zeiss) at 40x magnification.

## **CODEX staining**

5μm slices of murine young and nephritic kidneys were prepared and used for CODEX staining following manufacturer's instructions (Akoya Biosciences). Briefly, sections were retrieved from the freezer, let dry on Drierite beads and subsequently fixed for 10 min in ice-cold acetone. Samples were rehydrated in hydration buffer and photobleached twice for 45min as previously described <sup>51,52</sup>. After photobleaching, sections were blocked and stained with a 28-plex CODEX antibody panel overnight at 4°C. The following antibodies were used: anti-CD11b (Clone M1/70, BioLegend), anti-CD11c (Clone N418, BioLegend), anti- CD169 (Clone 3D6.112, BioLegend), anti- CD172a (Clone P84, BioLegend), anti- CD26 (Clone H194-112, BioLegend), anti- CD31 (Clone MEC13.3, BioLegend), anti- CD4 (Clone RM4-5, BioLegend), anti- CD44 (Clone IM7, BioLegend), anti- CD45 (Clone 30-F11, BioLegend), anti- CD8a (Clone 53-6.7, BioLegend), anti- CD90.2 (Clone 53-2.1, BioLegend), anti- EpCAM (Clone G8.8, BioLegend), anti- F4/80 (Clone

BM8, Thermo Scientific), anti- Ly6C (Clone HK1.4, Biolegend), anti- Ly6G (Clone 1A8, BioLegend), anti- MHCII (Clone M5/114.15.2, BioLegend), anti- NKp46 (Clone 29A1.4, BioLegend), anti- SiglecF (Clone 1RNM44N, Thermo Scientific), anti- TCRb (Clone H57-597, BioLegend), anti- XCR1 (Clone ZET, BioLegend), anti- CX3CR1 (Clone SA011F11, BioLegend), anti-SMA (Clone 1A4, BioLegend), anti-CD64 (Clone X54-5/7.1, BioLegend), anti-IBA1, (Clone EPR16589, Abcam), anti- ApoE (Clone EPR19392, Abcam), anti- CD206 (Clone MR5D3, BioRad) and anti- Nephrin (Clone AF31-59SP, R&D systems). After staining, samples were washed with staining buffer, fixed with ice-cold methanol, washed with 1x PBS and fixed with BS3 fixative (Sigma Aldrich, St. Louis, MO, USA). A final washing

### **CODEX** imaging, processing and analysis

of 1 week in CODEX storage buffer (Akoya Biosciences).

Prior to imaging, stained coverslips were equilibrated at room temperature. A multicycle CODEX experiment was performed following manufacturer's instructions (Akoya Biosciences). Images were acquired with a Zeiss Axio Observer widefield fluorescence microscope using a 20x objective (NA 0.85). A total of 10 slices with a z-spacing of 1.5 µm were acquired. The 405, 488, 568, and 647 nm channels were used. Raw files were exported using the CODEX Instrument Manager (Akoya Biosciences, Marlborough, MA, USA) and processed with CODEX Processor v1.7 (Akoya Biosciences).

step with 1x PBS was performed and samples were stored at 4°C before imaging for a maximum

To quantify the macrophage distribution, images were exported to QuPath <sup>53</sup>. Activated and non-activated tubules were identified based on the expression of EpCAM, CD44 and MHCII. Arterioles

were identified based on the co-expression of CD31 and SMA and glomeruli were delineated using Nephrin signals. Several of these anatomical areas were randomly selected in the medulla and cortex and a 10µm radius was drawn around them. Cells were detected and single object classifiers were implemented to identify the different cell types in the annotated areas. The total number of cells (for each cell type) per area was quantified.

## **Quantitative real time PCR from renal cortex**

The kidney cortex was dissected and snap-frozen in liquid nitrogen. After homogenizing of the tissue with UltraTurrax (VWR, 431-0179) in RLT buffer, total RNA was extracted using the RNeasy mini kit with on-column DNase digestion (Qiagen, 74106 and 79254) and 2 μg total RNA was reverse-transcribed using a High-Capacity cDNA Reverse Transcription Kit with RNase Inhibitor (Thermo Fisher Scientific, 4374966). 60 ng cDNA per reaction were subsequently subjected to real-time PCR. qRT-PCR reactions were performed using SYBR Green Select (Thermo Fisher Scientific, 4472908) and the following primers: *Gapdh* FW 5′ TGGAGAAACCTGCCAAGTATG, RV 5′ GTTGAAGTCGCAGGAGACAAC, *Trem2* FW 5′ TCCAGATCCTCACTGGACCC, RV 5′ TCCTGCTCCCAGGATAGGTG, *Csf2* FW 5′ TGCCTGTCACGTTGAATGAAG, RV 5′ GTGTTTCACAGTCCGTTTCCG and *Havcr1* (*Kim-1*) FW 5′ AAACCAGAGATTCCCACACG, RV 5′GTCGTGGGGTCTTCCTGTAGC. qRT-PCR was performed with the StepOnePlus Real-Time PCR Systems (Thermo Fisher). Relative amounts of mRNA were calculated by the ΔΔCt method using GAPDH as an internal control.

#### Measurement of blood urea nitrogen (BUN), albumin / creatinine ratio

Urine albumin (Albuwell M (m Albumin ELISA, Strip Plate, Ethos Biosciences, Inc., 1011) and urine creatinine (The Creatinine Companion (h,m,r microplate, Ethos Biosciences, Inc., 1012), serum blood urea nitrogen (BUN) (Urea Nitrogen Colorimetric Detection Kit, Thermo Fisher, EIABUN) were measured according to the kit manufacturer's instructions. All measurements were carried out using SpectraMax Plus (Molecular Devices) and analyzed using SoftMaxPro.

#### anti-double stranded DNA ELISA

To measure anti-dsDNA antibody levels in the serum, measurement plates were pre-coated with poly-Lysin (Sigma, P1274) for 1 hour at 37°C followed by DNA (Calf Thymus-DNA, Calbiochem, 2618) in TE-Buffer overnight at 4°C in the fridge. After blocking with 2% FBS in PBS, samples were diluted 1:100 in blocking buffer and incubated at room temperature for 2 hours, followed by incubation with Goat anti-mouse IgG (Fc)-HRPO, diluted in blocking buffer 1:10.000 (Dianova Cat# 115-035.071) for 1 hour. ABTS (2,2'-azino-di-(3-ethylbenzthiazoline sulfonic acid)) (Roche, Cat# 11684302001) was used as substrate. All measurements were carried out with SpectraMax Plus (Molecular Devices) and analyzed with SoftMaxPro.

## Preparation of single cell suspensions for whole kidney scRNA-seq

Female NZB/W F1 were analyzed at 12 ('young') and 25 weeks of age ('age-matched'). 25 weeks old mice were pre-treated with poly (I:C) ('nephritis'), or with poly (I:C) and anti-asialoGM1 antibodies ('aAGM1') to deplete NKp46<sup>+</sup> ILC. Whole kidney single cell suspensions were prepared as previously described, (https://www.protocols.io/view/p1-kidney-cold-active-protease-single-cell-dissoci-kqdg3o6pg25z/v1) with slight modifications. Briefly, kidneys were isolated in ice-cold PBS and minced on a petri dish on ice. 25 mg of kidney tissue was added to 1 ml of

protease solution (5 mM CaCl<sub>2</sub>, 10 mg/ml *Bacillus licheniformis* protease, and 125 U/ml DNase, incubated on ice and triturated every 2 min using a 1 ml pipet. After 11 min, digested tissue was passed through a 40 μm filter, rinsed with 1% BSA in PBS, and transferred to a new tube to which 1 ml of protease solution was added. The mix was further digested in a thermomixer at 1100RPM at 4°C with titruration every 2 min on ice. After 19 min, the mix was passed through a 30 μm filter, rinse with 1% BSA in PBS, and subjected to a third and fourth round of digestion in a thermomixer at 1200RPM and 1400RPM at 4°C. During the third (29 min) and fourth (40 min) digestion the mixture was triturated every 3 minutes using a 18G needle. After the fourth digestion, and another trituration and filtering through a 30 μm filter, the digested tissue was rinsed with 1% BSA in PBS, centrifuged and resuspended in RBC lysis buffer. Following titruration and 2 min incubation on ice, the digested tissue was washed and resuspended in 1% BSA in PBS. The single cell suspensions were visually inspected under the microscope to check cell integrity.

#### Preparation of kidney single cell suspensions for flow cytometry and sorting

Kidneys were harvested, minced and placed into RPMI 1640 Medium with GlutaMAX (Gibco) with collagenase IV (Worthington Biochemical, 570 U/ml) and DNase I (Roche, 12,5 U/ml). Tissue digestion was performed using the gentleMACS<sup>TM</sup> Dissociator and incubation with the enzymes at 37°C for 20 minutes. Single cell suspensions were obtained by passing cells through a 70-μm and 40-μm strainer and washing once with flow cytometry buffer. Following centrifugation at 500g for 5 minutes at 4°C, erythrocytes were removed by incubation in Red Blood Cell Lysing Buffer Hybri-Max<sup>TM</sup> (Sigma-Aldrich) or by centrifugation in Percoll gradient. For sorting of NKp46<sup>+</sup> ILC or Lin-NK1.1<sup>+</sup> ILC, leukocytes were further enriched by Percoll gradient

centrifugation (Cytiva). The pellet was resuspended in 40% Percoll layered over 80% Percoll prior to density centrifugation (1306g 20 min at 20°C with no brake).

Single-cell suspensions were plated in 96-well V-bottom plates on ice. FcγRIII/II were blocked with purified anti-CD16/32 (FcγRIII/II, eBioscience, 1:250) for 15 minutes at 4°C. Antibody mixes were added and incubated at 4°C in the dark for 30 minutes, then incubated with streptavidin conjugates for 20 minutes. Dead cells were excluded with either DAPI (eBioscience) or Fixable Viability Dye (FVD; eBioscience). Flow cytometry was performed using a BD Biosciences LSRFortessa or BD FACSymphony A5 flow cytometer and the BD Diva software (BD Bioscience). Cell sorting was performed using a BD Biosciences FACSAria II cell sorter achieving a purity rate of > 98%. Flow cytometry data were acquired using FACS Diva software v8.0.1 (BD Bioscience) and the data obtained were analyzed using FlowJo v10.10 (Flow Jo, BD Biosciences).

For intracellular staining of Eomes, cells were fixed at 4°C overnight and permeabilized for 1h at 4°C. Following fixation and permeabilization, cells were stained at 4°C with antibodies against Eomes in permeabilization buffer (1:100).

For intracellular staining of CSF2, live CD45<sup>+</sup> lineage (CD3, CD5, CD19, Ly6G)<sup>-</sup> NK1.1<sup>+</sup> cells were sorted with BD FACS Aria, treated with IL-2 (10 ng/mL) and IL-7 (10ng/ml) in complete RPMI overnight and then stimulated *ex vivo* with IL-2 (50 ng/mL, Peprotech), IL-7 (20 ng/mL, Peprotech), IL-12 (50 ng/mL, Miltenyi) plus IL-18 (50 ng/mL, R&D) for 6h in either purified anti-NKp46 antibody (BioLegend, Cat. 137602) or isotype (rat IgG2a, BioXCell, #BE0089) coated wells. BD GolgiPlug (including Brefeldin A) and BD Golgi Stop (4μL / 6mL) were added in the

medium after 1h. Cells were then fixed for 1h and permeabilized for 1 h at 4°C. Following fixation and permeabilization, cells were stained at 4°C with antibodies against CSF2 in permeabilization buffer (1:100).

794

795 The following antibodies were used for cell-surface staining: CD49b-FITC (DX5), MHC Class II 796 (I-A/I-E)-FITC (M5/114.15.2), CD11c-PerCP-Cyanine 5.5 (N418), CD335 (NKp46)-PerCP-797 Cyanine 5.5 (29A1.4), CD11b-PE-Cyanine 7 (M1/70), NK1.1-PE-Cyanine 7 (PK136), CD45-APC-798 eFluor780 (30-F11), CD3e-Biotin (145-2C11), CD5-Biotin (53-7.3), CD19-Biotin (MB19-1), 799 CD335 (NKp46)-Biotin (29A1.4), CD335 (NKp46)-PE-Cyanine 7 (29A1.4), CD49b-APC (DX5), 800 NK1.1-Super Bright 702 (PK136), MHCII-APC-eFluor® 780 (M5/114.15.2), CD11b-APC-801 eFluor® 780 (M1/70), CD45.2-FITC (104), MHCII - Super Bright<sup>TM</sup> 600 (M5/114.15.2), CD45-802 PerCP-Cyanine 5.5 (30-F11), F4/80-FITC (BM8), CD45.2-PE (MP1-22E9), CD45.2-APC (104), 803 CD45.2-PE (104), F4/80-eFluor®660 (BM8), CD16/32 (FcyRIII/II)-Purified (93) all from 804 eBioscience, CD62L-APC (clone MEL-14), anti-Ly-6G-Biotin (1A8), asialoGM1-Alexa Fluor® 805 647 (Poly21460), CD49d-PE-Cyanine7 (R1-2), Ly6C - BV605 (clone HK1.4), Ly6C-BV711 806 (HK1.4), XCR-APC (ZET), XCR1-PeDazzle (ZET), CD45.2-BV711 (104) from BioLegend, and 807 CD43-BV786 (S7), F4/80-BUV395 (T45-2342), CD45 BV711 (30-F11) from BD Biosciences. 808 The following antibodies were used for intracellular staining: GM-CSF-PE (MP1-22E9), CD107a 809 (LAMP-1)-Alexa Fluor® 647 (1D4B), Eomes-eFluor® 660 (Dan11mag), Ki67-Alexa Fluor® 647 810 (B56).

811

812

813

NKp46<sup>+</sup> ILC in Fig. 1a were identified as CD45<sup>+</sup> Lineage (CD3/CD5/CD19/Ly6G)<sup>-</sup> NKp46<sup>+</sup> NK1.1<sup>+</sup> cells. For scRNA-seq analysis of kidney tissue NKp46<sup>+</sup> ILC (Fig. 2a-e, Extended Data

Fig. 5a-e), tissue NKp46<sup>+</sup> ILC were sorted from 10 healthy young, 8 nephritic and 6 anti-NKp46-treated NZB/W F1 mice (gating strategy shown in Extended Data Fig. 5a-b). For the quantification of the percentage of CSF2<sup>+</sup> cells among CD49b<sup>-</sup> NKp46<sup>+</sup> ILC (Fig. 3a) one 'young' sample was pooled from 3 young mice; two of the 3 'nephritic' samples correspond each to one nephritic mouse, the third 'nephritic' sample was pooled from 2 nephritic mice. For scRNA-seq analysis of kidney leukocytes (Fig. 4f-g, Extended Data Fig. 8a-b), kidney leukocytes, including vessel-associated (CD45.2i.v.<sup>+</sup>) NK cells were isolated from 2 nephritic and 3 anti-NKp46 treated NZB/W F1 mice (gating strategy shown in Extended Data Fig. 8a). For scRNA-seq analysis of tNKp46<sup>+</sup> ILC (Extended Data Fig. 6e-j), we isolated tissue (CD45.2i.v.<sup>-</sup>) NKp46<sup>+</sup> ILC from 12 untreated and 8 poly(I:C)-treated RORgt-FM mice. For bulk RNA-seq analysis of kidney MΦ subsets (Extended Data Fig. 8c), kidney CD11b<sup>low</sup> MHC II<sup>high</sup> MΦ were isolated from 2 young NZB/W F1 mice; CD11b<sup>high</sup> MHC II<sup>high</sup> MΦ from 3 and CD11b<sup>high</sup> MHC II<sup>low</sup> MΦ and tissue F4/80<sup>low</sup> MHCII<sup>low</sup> monocytes from 4 nephritic NZB/W F1 mice.

#### **Degranulation and Cytotoxicity assay**

For CD107a surface stain (degranulation assay) of kidney NKp46<sup>+</sup> ILC and spleen NK cells, cells were incubated overnight at 37°C with IL-2 (20 ng/mL, Peprotech). IL-2 concentration was then increased to 50 ng/mL, apoptotic B16F10 cells and anti-CD107a (BioLegend) was added and incubated at 37°C for 4 hours. Cells were further incubated with Momensin (BD GolgiStop<sup>TM</sup>) before surface marker stain. To test the blocking activity of mNCR1.15 in a conventional killing assay, NKp46 ligand-expressing RMA-S cells were labelled with 5 μM CFSE for 10 min at 37°C, and extensively washed. NK cell frequencies in splenocyte suspensions from C57BL/6 mice were determined using flow cytometry. 10,000 CSFE-labelled RMA-S were mixed with splenocytes so

that an NK:effector ratio of 4:1 was achieved. To block NKp46 receptor-ligand interactions 10 µg/mL NKp46 (mouse IgG1) or control Ab (KIR2DL1.03, mouse IgG1, kappa) were added to the assay. Cells were incubated in triplicates for 4 hours in a humidified atmosphere of 5% CO<sub>2</sub> and 37°C and in the presence of 100 U/ml IL-2. Cells were then harvested and analyzed. The percentage of specific lysis was calculated as follows: [mean % of viable CFSE<sup>+</sup> target cells incubated with effectors] - [mean % of viable CFSE<sup>+</sup> target cells without effectors] / 100 - [mean % of viable CFSE<sup>+</sup> target cells without effectors] × 100.

### bulk RNA-seq library preparation and sequencing

Gene expression library preparation was performed using total RNA from 2 samples from cells pooled from 2 young mice and 5 samples from 1 nephritic mouse each, with 15,000 to 20,000 cells per sample. RNA quality was determined on a Fragment Analyzer using the HS RNA 15nt Kit (Agilent Technologies). For poly-A dependent cDNA synthesis and a first amplification step the Smart-Seq v4 mRNA Ultra Low Input RNA Kit (Clontech) was used with 100 pg RNA input and according to the manufacturer's instructions. After quality control (HS NGS Fragment Kit (1-6000bp), Agilent) and concentration measurement (Qubit dsDNA HS Assay Kit, Invitrogen), 3 ng of the purified cDNA were used for library completion with the Nextera XT library preparation kit (Illumina). Quality and quantity of the final sequencing libraries was again assessed with the tools mentioned for intermediate analysis. In the following, 2x59 nt paired-end sequencing was performed on an Illumina NextSeq2000 using a P1 flow cell (100 Cycles).

After sequencing and mapping (refdata-gex-mm10-2020-A, 10xGenomics), Fragments per kilobase million (FPKM) were computed based on the count matrices. Principal Component

Analysis (PCA) was performed using DESeq2. The web version of ClustVis <sup>54</sup> was used to generate heatmaps from this dataset.

#### scRNA-seq library preparation and sequencing

Isolated single cells were counted using a Countess<sup>TM</sup> II automated cell counter (Life Technologies) after trypan blue staining using at least two separate counts. The cell suspension was loaded on Chromium Controller (10X Genomics) with a targeted cell recovery of 10,000 per reaction. For whole kidneys, 3' gene expression libraries were prepared using v3 Chromium Single Cell reagent or Next GEM Single Cell 3' GEM Kit v3 (10X Genomics) according to the manufacturer's instruction. For kidney NKp46<sup>+</sup>NK1.1<sup>+</sup> ILC, 5' gene expression libraries were generated using Chromium Next GEM Single Cell 5' Kit v2 (10X Genomics) according to the manufacturer's instruction. Quality control of cDNA and final libraries was done using Bioanalyzer High Sensitivity DNA Analysis (Agilent) and the KAPA library quantification kit. Libraries were sequenced using HiSeq 4000 (Illumina) or NextSeq 2000 (Illumina).

# Computational analysis of scRNA-seq data

## Transcriptome mapping

After sequencing, the sequence data were mapped to the mouse reference genome (mm10 pre-built references v 3.0.0) provided by 10X Genomics using the CellRanger suite (v.3.0.1). The count matrices generated by CellRanger as follows were used for the further analysis. Mapping quality was assessed using the CellRanger summary statistics.

#### **Empty droplets removal and doublet estimation**

Empty droplets were identified by Emptydrops, which is implemented in the CellRanger workflow. After removal of empty droplets, we applied scrublet per sample<sup>55</sup> to assign a doublet score (scrublet\_score) to the metadata container of each cell.

885

886

887

888

889

890

891

892

893

894

895

896

897

898

899

900

901

902

903

904

882

883

884

#### Cell quality control and filtering

Downstream analysis employed the concatenated filtered feature-barcode matrices, using Seurat<sup>56</sup>. Genes were filtered out when they were expressed in less than three cells. We applied two sets of cell filtering criteria due to data quality differences between the technical batches. The filtering cut-off was decided based on the distribution of data quality and the estimated doublet ratio provided by 10X Genomics (in case of 10,000 targeted recovery, the estimated doublet ratio is up to 8%). For the analysis of the first batch of the whole kidney dataset (H 01, D 01 and T 01), cells were filtered for counts (nCount RNA < 30,000), genes (500 < nFeature RNA < 6,000), mitochondrial genes (percent.mt < 75%), ribosomal genes (percent.ribo < 30%) and scrublet score (scrublet score < 0.2). For the rest of whole kidney dataset, cells were filtered for counts (nCount RNA < 20,000), genes (500 < nFeature RNA < 4,000), mitochondrial genes (percent.mt < 75%), ribosomal genes (percent.ribo < 30%) and scrublet score (scrublet score < 0.2). For NZB/W and RORgt-FM kidney NK1.1<sup>+</sup> NKp46<sup>+</sup> ILC, cells were filtered for counts (nCount RNA < 15,000), genes (300 < nFeature RNA < 4,000), mitochondrial genes (percent.mt < 3%), ribosomal genes (percent.ribo < 30%) and scrublet score (scrublet score < 0.2). 8-11% of the lowquality cells and estimated doublets per sample were filtered out. For the dataset of kidney leukocytes and vessel-associated NK cells, cells were filtered for counts (nCount RNA < 20,000), genes (300 < nFeature RNA < 5,000), mitochondrial genes (percent.mt < 5%), ribosomal genes (percent.ribo < 45%) and scrublet score (scrublet score < 0.05). For human leukocytes, cells were

filtered for counts (nCount\_RNA < 600,000) and genes (nFeature\_RNA < 6,000). After filtering and quality control, the resulting datasets included: a) 74,850 whole kidney cells, isolated from 3 young, 3 age-matched, 3 nephritic and 3 anti-AGM1-treated NZB/W F1 mice; b) 17,766 tissue NKp46<sup>+</sup> ILC isolated from 10 young, 8 nephritic and 3 anti-NKp46 treated NZB/W F1 mice; c) 8,396 tissue NKp46<sup>+</sup> ILC from 12 untreated and 8 poly(I:C)-treated RORgt-FM mice; d) 18,972 kidney leukocytes and vessel-associated NK cells, isolated from 2 nephritic and 3 anti-NKp46 treated NZB/W F1 mice.

## Dimensionality reduction, clustering, and analysis of differentially expressed genes

After read count normalization and log-transformation, top 2000 highly variable genes were selected. Prior to manifold construction using UMAP, top 20 principal components were harmonized by anchored canonical correlation analysis (CCA)<sup>57</sup>. Cells were clustered using the original Louvain algorithms. DEGs per cluster were calculated using *FindMarkers* function of Seurat with the Wilcoxon rank sum test. For the marker gene computation, we selected genes expressed in at least 25% of cells in either of the populations and with a log<sub>2</sub>-transformed fold change of at least 0.25. Genes with adjusted p-value < 0.05 were called as marker DEGs. Cell type/states annotation was performed based on those results and manually selected canonical marker gene expression.

# Analysis of differentially expressed genes within a cluster and gene ontology term analysis

DEGs within subsets of a cluster were calculated using the *FindMarkers* function of Seurat with the Wilcoxon rank sum test by default settings. For the marker gene computation, we selected genes expressed in at least 10% of cells in either of the populations and with a log<sub>2</sub>-transformed

fold change of at least 0.25. Genes with adjusted p-value < 0.05 were called DEGs. For GO term analysis within clusters, DEGs were used as input for g:Profiler functional profiling.

# Computation of an NKp46 activation signature

Using a previously published gene set<sup>37</sup>, we calculated a gene signature score by applying the function *AddModuleScore* from Seurat including genes that were detectable in our dataset.

#### Identification of genes coregulated with *Trem2* in immune cells

To find genes coregulated with *Trem2* in immune cells, raw sum counts matrices (pseudo-bulk count matrices) were calculated per immune cell cluster per sample. Fragments per kilobase million (FPKM) were computed based on the pseudo-bulk count matrices. Protein-coding genes with FPKM >1 were used for the further analysis. DESeq2-normalized counts of pairwise complete observations were computed from the pseudo-bulk raw count. Samples with zero counts for a specific gene were excluded from the correlation calculations. Spearman correlations were calculated to test for coregulation using the DESeq2-normalized counts. Genes with the absolute of correlation coefficient (r) > 0.5 and adjusted p-value < 0.05 were called significantly coregulated genes.

# Identification of modules of genes differentially expressed across cellular trajectories

To generate cellular trajectories (pseudotemporal dynamics) we used the *monocle3* R package<sup>58</sup>. We ordered cells in a semi-supervised manner based on their *Seurat* clustering. Differentially expressed genes across the pseudotime trajectory were computed by graph\_test function of *monocle3* and genes with Moran's I test  $\geq 0.1$  and FDR < 0.05 were called differentially expressed.

Modules were calculated by the find\_module\_gene function implemented by monocle3 with q-value < 0.05.

953

954

955

956

957

958

959

960

961

962

963

951

952

# Differentiation trajectory analysis by RNA velocity analysis

In order to estimate cell velocities from their spliced and unspliced mRNA content, referred to RNA velocity, we initially used the *velocyto* python package v0.13 (whole kidney)<sup>59</sup> to recover spliced and unspliced read-counts from the bam files from CellRanger outputs per data set. Finally, the scVelo package (version 0.2.4) was employed to translate the unspliced-spliced ratios into velocities and visualize the result. The analysis was conducted according to the "dynamical" model implementation, described in the respective online tutorial as (https://scvelo.readthedocs.io/DynamicalModeling/). Aggregated velocity fields and transition probabilities per subpopulations were visualized on UMAP representations generated by the Seurat-pipeline.

964

965

966

967

968

969

970

971

972

## Statistical analysis, visualization and reproducibility

Statistical analysis was performed using Graphpad Prism 10 or R (v4.1.2). Dot, violin and feature plots were created using *Seurat* implemented functions. Heatmap were generated using ComplexHeatmap v 2.13.0, ggplot2 v 3.3.6, pheatmap v 1.1.12 and gplots v 3.1.3.

Statistical tests used are indicated in the figure legends. Paired or unpaired t-test or Mann-Whitney test at 95% confidence interval was performed for comparisons between two groups, as indicated in the figure legends. For real-time PCR, biochemical assays, and flow cytometric quantifications comparing more than two groups, one-way ANOVA followed by Tukey's test at 95% confidence

- 973 interval was performed. Areas positive for a marker by histology were compared using Kruskal-
- Wallis test followed by Dunn's multiple comparisons, as indicated in the figure legends.

975

976

## Data availability

- 977 The data will be available for download under the following repositories: European Nucleotide
- 978 Archive at EMBL-EBI, accession number PRJEB54636 (whole kidney scRNA-seq); Gene
- 979 Expression Omnibus, accession number GSE207139 (kidney NKp46<sup>+</sup> ILC scRNA-seq), accession
- 980 number GSE269399 (kidney CD45+ scRNA-seq), accession number GSE269400 (kidney ILC
- 981 RORgtfm scRNA-seq) and accession number GSE269402 (kidney macrophage bulk RNA-seq).
- 982 Re-analysis of leukocyte scRNA-seq derived from human lupus nephritis biopsies was done on
- 983 the dataset from Arazi et al<sup>3</sup>, which is publicly available found in the database of Genotypes and
- 984 Phenotypes (dbGaP) (accession code phs001457.v1.p1)

985

- 986 39 Arnold, S. J., Hofmann, U. K., Bikoff, E. K. & Robertson, E. J. Pivotal roles for 987 eomesodermin during axis formation, epithelium-to-mesenchyme transition and endoderm 988 specification the mouse. Development 135, 501-511 (2008).in 989 https://doi.org:10.1242/dev.014357
- 990 40 Grote, D. *et al.* Gata3 acts downstream of beta-catenin signaling to prevent ectopic metanephric kidney induction. *PLoS Genet* 4, e1000316 (2008). <a href="https://doi.org:10.1371/journal.pgen.1000316">https://doi.org:10.1371/journal.pgen.1000316</a>
- 993 41 Narni-Mancinelli, E. *et al.* Fate mapping analysis of lymphoid cells expressing the NKp46 cell surface receptor. *Proc Natl Acad Sci U S A* **108**, 18324-18329 (2011). https://doi.org:10.1073/pnas.1112064108
- Eberl, G. & Littman, D. R. Thymic origin of intestinal alphabeta T cells revealed by fate
   mapping of RORgammat+ cells. Science 305, 248-251 (2004).
   <a href="https://doi.org:10.1126/science.1096472">https://doi.org:10.1126/science.1096472</a>
- 999 43 Srinivas, S. *et al.* Cre reporter strains produced by targeted insertion of EYFP and ECFP into the ROSA26 locus. *BMC Dev Biol* 1, 4 (2001). <a href="https://doi.org:10.1186/1471-213x-1-1001">https://doi.org:10.1186/1471-213x-1-1001</a>
- Arnold, S. J., Sugnaseelan, J., Groszer, M., Srinivas, S. & Robertson, E. J. Generation and analysis of a mouse line harboring GFP in the Eomes/Tbr2 locus. *Genesis* 47, 775-781 (2009). <a href="https://doi.org:10.1002/dvg.20562">https://doi.org:10.1002/dvg.20562</a>

- Morel, L. *et al.* Genetic reconstitution of systemic lupus erythematosus immunopathology with polycongenic murine strains. *Proc Natl Acad Sci U S A* **97**, 6670-6675 (2000). https://doi.org:10.1073/pnas.97.12.6670
- 1008 46 Subramanian, S. et al. A Tlr7 translocation accelerates systemic autoimmunity in murine 1009 (2006).lupus. Proc Natl Acad Sci IIA 103, 9970-9975 S 1010 https://doi.org:10.1073/pnas.0603912103
- 1011 47 Turnbull, I. R. *et al.* Cutting edge: TREM-2 attenuates macrophage activation. *J Immunol* 1012 177, 3520-3524 (2006). <a href="https://doi.org:10.4049/jimmunol.177.6.3520">https://doi.org:10.4049/jimmunol.177.6.3520</a>
- Glasner, A. *et al.* Expression, Function, and Molecular Properties of the Killer Receptor Ncr1-Noé. *J Immunol* **195**, 3959-3969 (2015). <a href="https://doi.org:10.4049/jimmunol.1501234">https://doi.org:10.4049/jimmunol.1501234</a>
- Gschwend, J. *et al.* Alveolar macrophages rely on GM-CSF from alveolar epithelial type 2 cells before and after birth. *J Exp Med* **218** (2021). <a href="https://doi.org:10.1084/jem.20210745">https://doi.org:10.1084/jem.20210745</a>
- Yona, S. *et al.* Fate mapping reveals origins and dynamics of monocytes and tissue macrophages under homeostasis. *Immunity* **38**, 79-91 (2013). <a href="https://doi.org:10.1016/j.immuni.2012.12.001">https://doi.org:10.1016/j.immuni.2012.12.001</a>
- Du, Z. *et al.* Qualifying antibodies for image-based immune profiling and multiplexed tissue imaging. *Nat Protoc* **14**, 2900-2930 (2019). <a href="https://doi.org:10.1038/s41596-019-0206-y">https://doi.org:10.1038/s41596-019-0206-y</a>
- Bayerl, F. *et al.* Guidelines for visualization and analysis of DC in tissues using multiparameter fluorescence microscopy imaging methods. *Eur J Immunol* **53**, e2249923 (2023). <a href="https://doi.org:10.1002/eji.202249923">https://doi.org:10.1002/eji.202249923</a>
- 1026 53 Bankhead, P. *et al.* QuPath: Open source software for digital pathology image analysis. *Sci* 1027 *Rep* 7, 16878 (2017). <a href="https://doi.org:10.1038/s41598-017-17204-5">https://doi.org:10.1038/s41598-017-17204-5</a>
- 1028 54 Metsalu, T. & Vilo, J. ClustVis: a web tool for visualizing clustering of multivariate data using Principal Component Analysis and heatmap. *Nucleic Acids Res* **43**, W566-570 (2015). <a href="https://doi.org/10.1093/nar/gkv468">https://doi.org/10.1093/nar/gkv468</a>
- Wolock, S. L., Lopez, R. & Klein, A. M. Scrublet: Computational Identification of Cell Doublets in Single-Cell Transcriptomic Data. *Cell Syst* 8, 281-291.e289 (2019). https://doi.org:10.1016/j.cels.2018.11.005
- 1034 56 Hao, Y. *et al.* Integrated analysis of multimodal single-cell data. *Cell* **184**, 3573- 3587.e3529 (2021). <a href="https://doi.org:10.1016/j.cell.2021.04.048">https://doi.org:10.1016/j.cell.2021.04.048</a>
- 1036 57 Stuart, T. *et al.* Comprehensive Integration of Single-Cell Data. *Cell* **177**, 1888-1902 e1821 (2019). <a href="https://doi.org/10.1016/j.cell.2019.05.031">https://doi.org/10.1016/j.cell.2019.05.031</a>
- 1038 58 Cao, J. *et al.* The single-cell transcriptional landscape of mammalian organogenesis.

  1039 *Nature* **566**, 496-502 (2019). <a href="https://doi.org:10.1038/s41586-019-0969-x">https://doi.org:10.1038/s41586-019-0969-x</a>
- 1040 59 La Manno, G. *et al.* RNA velocity of single cells. *Nature* **560**, 494-498 (2018). 1041 <a href="https://doi.org:10.1038/s41586-018-0414-6">https://doi.org:10.1038/s41586-018-0414-6</a>

#### 1044 ACKNOWLEDGMENTS

1043

- We thank Eric Vivier, Chiara Romagnani, Georg Gasteiger, Lukas Amann, Marco Prinz, Thomas
- Winkler and Andrey Kruglov for mouse lines and helpful discussions, and Eicke Latz and Andreas

1047 Radbruch for continuous support. The work was supported by the European Research Council 1048 (ERC StG 805143 DDRMac to A.T.; ERC AdG 101055309 to A.D.; ERC AdG 788970 to N.H.) 1049 and by the German Research Foundation (DFG) (SPP1937/428195445 to A.T. and K.T., SFB 1050 1444/427826188 and TRR 241/375876048 to A.T. and A.D., SPP1937/Di764 ILCAdapt /9-2 to 1051 A.D.; SPP1937/HA5354/8-2/320406065 and SFB1444 P14/427826188 to A.E.H.; TRR 1052 167/259373024 and TR 84/114933180 to A.T., SFB 1160/256073931 to A.T. and R.V., and STA 1053 1657/2-1 to EGS). M.F.M was supported by grants from the Leibniz Association (Leibniz 1054 Collaborative Excellence, TargArt and ImpACt) and the German Federal Ministry of Education 1055 and Research (BMBF, CONAN, TreAT, 01GL2401C). C.S. is supported by the Peter Hans 1056 Hofschneider Professorship for Molecular Medicine. N.H. is supported by the Chan Zuckerberg 1057 Foundation (2019-2026), the Leducq Foundation (16CVD03), the British Heart Foundation and 1058 Deutsches Zentrum für Herz-Kreislauf-Forschung (BHF/DZHK: SP/19/1/34461) and the 1059 Deutsche Forschungsgemeinschaft (SFB1470, B03). M.K. received funding provided by the 1060 Alexander von Humboldt Foundation and SENSHIN Medical Research Foundation.

1061

1062

1063

1064

1065

1066

1067

1068

1069

#### **AUTHOR CONTRIBUTIONS**

S.I. B.G. performed the majority of the experiments and scRNA-seq data analysis and prepared most figures of the manuscript. T.A. performed the first line of experiments characterizing kidney ILC populations and showing a role of NKp46<sup>+</sup> ILC in lupus nephritis. K.S. performed the *Sle1Yaa;Trem2*-/-, *Ncr1*<sup>Gfp/Gfp</sup> Imiquimod, anti-CSF2, NKp46 stimulation, *Csf2*-TdTomato, CX3CR1<sup>CreERT2</sup>R26<sup>TdTom</sup>, and CD45.2*i.v.* tracking experiments and all experiments for manuscript revisions. A.Ta., V.J., T.K., A.K., L.F., M.P., G.M.G., assisted with experiments. F.S. (IF/confocal microscopy, ELISAs, qPCRs), F.H., P.D. G.P., E.L-H.L. and H.M. (bioinformatics), D.B. and A.S.

1070 (CODEX), performed experiments and/or analyzed data as indicated. C.S., I.M., M.M., J.H., 1071 K.W.H., O.H., A.M., A.J.C., A.E.H., M.C., G.K. and R.E.V. provided protocols and critical 1072 reagents or mouse lines. M.-F.M. and K.T. oversaw bioinformatics analysis of ILC. A.D. and S.J. 1073 gave critical input on NKp46<sup>+</sup> ILCs. A.T. and M.K. directed the research, supervised experiments 1074 and data analysis and, together with A.D. wrote the manuscript with input from all co-authors.

1075

1076

1077

#### **DECLARATION OF INTERESTS**

The authors declare no competing interests.

1078

1079

1080

1081

1082

1083

1086

1087

1088

1090

1091

1092

# **Extended Data Figure Legends**

Extended Data Figure 1. Regulation and role of tissue NKp46<sup>+</sup> ILC in lupus nephritis. a, Experimental set-up for anti-IFNAR1 treatment, related to b-e. b, Quantification of urine Albumin/Creatinine Ratio. (left to right: n = 8, 10, 9, 10 mice per group), pooled from 2 independent experiments. c, Left: Representative flow cytometry plots of kidney leukocytes 1084 (CD45<sup>+</sup>). The gates indicate tissue (CD45.2*i.v.*<sup>-</sup>) and vessel-associated (CD45.2*i.v.*<sup>+</sup>) leukocytes. 1085 Right: Quantification of tissue and vessel-associated leukocytes (left to right: n = 4, 5, 5, 5 mice per group), representative of 2 independent experiments. d, Kidney NKp46<sup>+</sup> ILC subsets of tissue CD49b<sup>+</sup> (red), tissue CD49b<sup>-</sup> (orange) and vessel-associated CD49b<sup>+</sup> (blue) in young non-nephritic and poly (I:C) nephritic kidneys were analyzed for Eomes expression. e, left: Kidney leukocytes 1089 were gated on CD45<sup>+</sup> Lineage (CD3/CD5/CD19/Ly6G)<sup>-</sup> NKp46<sup>+</sup> NK1.1<sup>+</sup> cells (i.e., NKp46<sup>+</sup> ILC). Representative flow cytometry plots of kidney NKp46<sup>+</sup> ILC are shown. The black gate indicates tissue (CD45.2i.v.) NKp46<sup>+</sup> ILCs. Right: Quantification of kidney tissue NKp46<sup>+</sup> ILC (left to right: n = 4, 5, 5, 5 mice per group), representative of 3 independent experiments. f, Left:

Representative flow cytometry plots of kidney NKp46<sup>+</sup> ILC analyzed for CD49b and CD45.2i.v., indicating tissue CD49b<sup>+</sup>, tissue CD49b<sup>-</sup> and vessel-associated CD49b<sup>+</sup> subsets from untreated and poly (I:C)-treated Eomes<sup>flox/flox</sup> and Eomes<sup>flox/flox</sup>; Ncr1<sup>iCreTg</sup> mice. Right: Quantification of tissue CD49b<sup>-</sup>, tissue CD49b<sup>+</sup> and vessel-associated NKp46<sup>+</sup> ILC (n = 4, 3, 3, 3 mice per group), representative of 2 independent experiments. g, Top: Representative flow cytometry plots of kidney CD45<sup>+</sup> Lineage (CD5/CD3/CD19/Ly6G)<sup>-</sup> NKp46<sup>+</sup> ILC analyzed for CD49b, CD45.2i.v., indicating tissue CD49b<sup>+</sup>, tissue CD49b<sup>-</sup> and vessel-associated CD49b<sup>+</sup> subsets from poly (I:C)treated Gata3<sup>flox/flox</sup> and Gata3<sup>flox/flox</sup>; Ncr1<sup>iCreTg</sup> mice. Right: Quantification of tissue CD49b<sup>-</sup> and CD49b<sup>+</sup> NKp46<sup>+</sup> ILC (n = 3, 4 mice per group), representative of 2 independent experiments. **h**, Experimental set up for anti-AGM1 treatment, related to i, and Fig. 1a-c, l. i, Quantification bar chart of urine Albumin/Creatinine Ratio. (n = 9, 11, 11 mice per group), pooled from 2 independent experiments. i, Experimental set up for anti-AGM1 treatment in spontaneous nephritis, related to k. k, Quantification bar chart of urine Albumin/Creatinine Ratio (left) and serum BUN (middle). Renal cortex *Haver1* mRNA expression (right) analyzed by real-time PCR; values are relative to Gapdh. Relative mRNA expression of untreated young control kidneys was considered as 1. (n =4, 7, 6 mice per group for Albumin/Creatinine Ratio and Haver 1 and n = 4, 7, 5 mice per group for BUN). One-way ANOVA followed by Tukey's test (b, c, e-f, i, k) or two-tailed unpaired t-Test (g). The bars show mean  $\pm$  SD.

1111

1112

1113

1114

1115

1093

1094

1095

1096

1097

1098

1099

1100

1101

1102

1103

1104

1105

1106

1107

1108

1109

1110

Extended Data Figure 2. mNCR1.15 antibody shows NKp46 blocking activity. a, Experimental set-up for NKp46 blocking with mNCR1.15 in NZB/W F1 mice, related to b, c and Fig.1d-e. b, Downregulation of NKp46 from the cell surface of Lin-NK1.1+ ILC following treatment with mNCR1.15. Representative NKp46 antibody staining of kidney Lin-NK1.1+ ILC

normalized to mode (left) and quantification of mean fluorescence intensity (right) (n = 4, 4, 6, 4 mice per group).  $\mathbf{c}$ , Representative flow cytometry plots and quantification of kidney NKp46<sup>+</sup>ILC subsets (n = 4, 4, 6, 4 mice per group).  $\mathbf{d}$ , Experimental set-up for short term treatment of NZB/W F1 mice with mNCR1.15, or isotype control, related to e.  $\mathbf{e}$ , Quantification of kidney Lin NK1.1<sup>+</sup> cells (n = 4 mice per group).  $\mathbf{f}$ , RMA-S cells express NKp46 (NCR1) ligands. Representative staining (2 independent experiments) with NCR1-hIg fusion or irrelevant fusion protein, measured by flow cytometry.  $\mathbf{g}$ , Splenic NK cells were pre-incubated with mNCR1.15 or isotype control antibody. They were then mixed with RMA-S target cells in a 4:1 ratio. Quantification of target cell killling is shown.  $\mathbf{h}$ , Pre-incubation of the NCR1-hIG fusion protein with mNCR1.15 inhibits its binding to B16 target cells, unlike other NKp46-targeting antibody clones, such as mNCR1.22 or mNCR1.05, whose pre-incubation does not inhibit or only partially inhibits the binding of NCR1-hIG fusion protein to B16 target cells, respectively. Representative images of 3 independent experiments are shown. One-way ANOVA followed by Tukey's test ( $\mathbf{b}$ ,  $\mathbf{c}$ ) or two-tailed unpaired t-Test ( $\mathbf{e}$ ,  $\mathbf{g}$ ). The bars show mean  $\pm$  SD.

Extended Data Figure 3. Whole kidney scRNA-seq analysis of lupus nephritis. a, Fractions of kidney cell populations presented as percent of the whole kidney cells within each of the indicated experimental groups (n = 3 mice per group). b, Violin plots of canonical marker genes across kidney cell types. c, Dot plot of top 5 expressed genes across the kidney cell types shown in Figure 1f. Dot size indicates percentage of expressing cells (% Exp.) and color scale shows average expression level of log-normalized counts (Avg Exp.). d, Violin plots of canonical marker genes across the PEC/Podocyte subpopulations shown in Fig. 1g. e, Dot plot of top 5 expressed genes across the PEC/podocyte clusters shown in Figure 1g. Dot size indicates percentage of expressing

cells (% Exp.) and color scale shows average expression level of log-normalized counts (Avg Exp.).  $\bf f$ , Fractions of PEC/podocyte subpopulations presented as percent of all PEC/podocytes within each of the indicated conditions (n=3 mice per group).  $\bf g$ , UMAP embedding for the subcluster analysis of 44,077 single-cell transcriptomes of proximal tubular cells (n=3 mice per group).  $\bf h$ , Fractions of proximal tubular cell subpopulations presented as percent of all proximal tubular cells within each of the indicated conditions (n=3 mice per group).  $\bf i$ , Violin plots of canonical marker genes across proximal tubular cells.  $\bf j$ , Dot plot showing the expression levels of selected marker genes for the indicated proximal tubular cell clusters. Dot size indicates percentage of expressing cells (% Exp.) and color scale shows average expression level of log-normalized counts (Avg Exp.). One-way ANOVA followed by Tukey's test ( $\bf a$ ,  $\bf f$ ,  $\bf h$ ). The bars show mean  $\pm$  SD.

Extended Data Figure 4: Capillary endothelial cell de-differentiation in lupus nephritis. a, UMAP embedding for the subcluster analysis of 5,251 endothelial cells (EC). Annotation to EC subpopulations was based on Louvain clustering and expression of canonical marker genes. cEC, capillary EC; gEC, glomerular EC; artl-EC, arteriolar EC; DVR, descending vasa recta; art-EC, arterial EC; LN-EC, lupus nephritis-associated EC. b, Left: Distribution of each experimental group on UMAP embedding. Right: Fractions of EC subpopulations presented as percent of the whole kidney cells within each of the indicated experimental groups (n =3 mice per group). c, Violin plots of canonical marker genes across EC subpopulations. d, Dot plot of top 5 expressed genes across EC clusters shown in a. Dot size indicates percentage of expressing cells (% Exp.) and color scale shows average expression level of log-normalized counts (Avg Exp.). e, f, Volcano plot showing differentially expressed genes of cEC (e) or gEC (g) from nephritis vs young (left

panel) or nephritis vs aAGM1 treated (right panel). The intercepts of x dashed lines are -0.25 and +0.25. The intercept of y dashed lines is -log10(0.05). **g, h**, Selected pathways regulated by GO term analysis of differentially expressed genes in cEC and gEC in the indicated conditions (nephritis vs. young controls). **i**, Dot plot showing the expression levels of selected endothelial cell marker genes for LN-EC3. Dot size indicates percentage of expressing cells (% Exp.) and colour scale shows average expression level of log-normalized counts (Avg Exp.). **j**, CD31 (white) IF from kidney cortex, representative from 3 independent experiments. Green arrows point to long, thin peritubular capillaries. Blue arrows point to short intertubular vessels. Short yellow arrows point to glomerular areas devoid of capillaries. One-way ANOVA followed by Tukey's test (**b**) or cumulative hypergeometric test as implemented in the g:Profiler by default settings (**g-h**). The bars show mean ± SD.

# Extended Data Figure 5: scRNA-seq analysis of tissue NKp46<sup>+</sup> ILC.

**a-b**, Experimental set-up for scRNA-seq analysis related to a-e and Fig. 2. Samples were pooled from experiments 1 and 2. In experiment 1 kidney tissue NKp46<sup>+</sup> ILC were isolated from 10 young and 6 nephritic mice (nephritis 1). In experiment 2 kidney tissue NK1.1<sup>+</sup> ILC were isolated from 2 isotype-treated nephritic (nephritis 2) - and 3 anti-NKp46 (mNCR1.15)-treated mice. tILC, tissue 'helper' innate lymphoid cell; tNK, tissue natural killer cell. Left: Flow cytometry plots of kidney NKp46<sup>+</sup> ILC (a) and Lineage<sup>-</sup> NK1.1<sup>+</sup> ILC (b). The red gate indicates tissue (CD45.2*i.v.*-') cells that were isolated and sequenced. Middle: Distribution of each experimental group on UMAP embedding. Right: Fractions of kidney tissue NKp46<sup>+</sup> ILC (a) and Lin<sup>-</sup>NK1.1<sup>+</sup> ILC (b) presented as percent of tissue NKp46<sup>+</sup> tILC for tILC clusters and as percent of tissue NKp46<sup>+</sup> tNK for tNK clusters within each of the indicated experimental conditions. **c**, Dot plot of top 5 expressed genes

across tissue NKp46<sup>+</sup> ILC clusters shown in Fig. 2a. **d**, Violin plots show expression of canonical marker genes across tissue NKp46<sup>+</sup> ILC subpopulations shown in Figure 2a. Dot size indicates percentage of expressing cells (% Exp.) and color scale shows average expression level of lognormalized counts (Avg Exp.). **e**, Dot plot showing the expression levels of selected marker genes for the indicated tissue NKp46<sup>+</sup> ILC clusters. Dot size indicates percentage of expressing cells (% Exp.) and color scale shows average expression level of log-normalized counts (Avg Exp.). **f**, Representative flow cytometry plots of kidney NKp46<sup>+</sup> ILC and spleen NK cells, indicating CD107a expression in tissue vs vessel-associated subpopulations (n = 2 young and 4 nephritic mice).

## Extended Data Figure 6. NKp46<sup>+</sup> tILC in human lupus nephritis.

a, Left: Experimental set-up. Graphic created with Biorender. Right: UMAP embedding of 2,302 human leukocytes from 24 lupus nephritis patients and 10 controls<sup>28</sup> color-coded for T cell/ NKp46<sup>+</sup> ILC clusters. b, Violin plots of the indicated genes across human leukocyte subpopulations. c, Left: UMAP embedding of 341 NKp46<sup>+</sup> ILC, color-coded for NK cells (pink) and ILC1/NKp46<sup>+</sup> ILC3 subsets (turquoise). Right/Bottom: Feature plots of the indicated genes across human NKp46<sup>+</sup> ILC subpopulations. d, Left: Representative flow cytometry plots of kidney NKp46<sup>+</sup> ILC analyzed for Eomes and RORgt-FM. The gates indicate RORgt-FM<sup>+</sup> Eomes<sup>-</sup> ILC3 (green), RORgt-FM<sup>-</sup> Eomes<sup>-</sup> ILC1 (pink) and RORgt-FM<sup>-</sup> Eomes<sup>+</sup> NK cells (blue) in untreated and in RORgt-FM; Eomes-GFP reporter mice treated with poly (I:C). Vessel-associated (CD45.2*i.v.*<sup>+</sup>) (top row) and tissue (CD45.2*i.v.*<sup>-</sup>) (bottom row) NKp46<sup>+</sup> ILC were analyzed separately. Middle: Quantification of the fraction of ILC1, ILC3, and NK cells among vessel-associated (top) and tissue (bottom) NKp46<sup>+</sup> ILC. Right: Quantification of ILC1, ILC3, and NK

cells (*n* = 4 mice per group). **e**, UMAP embedding of 8,396 single-cell transcriptomes of kidney tissue NKp46<sup>+</sup> ILC colored by cell annotation. tILC, tissue innate lymphoid cell; tNK, tissue natural killer cell. **f**, Dot plot of top 5 expressed genes across the kidney tissue NKp46<sup>+</sup> ILC shown in b. Dot size indicates percentage of expressing cells (% Exp.) and color scale shows average expression level of log-normalized counts (Avg Exp.). **g**, Violin plots showing levels of expression of an NKp46 activation gene signature<sup>37</sup> across kidney tissue NKp46<sup>+</sup> ILC clusters. **h**, Composition of tissue NKp46<sup>+</sup> ILC per condition. **i**, Contribution of RORγt-FM<sup>+</sup> and RORγt-FM<sup>-</sup> cells to *Tnfrsf*9<sup>+</sup> tILC per condition. **j**, Violin plots showing levels of expression of an NKp46 activation signature<sup>37</sup> in *Tnfrsf*9<sup>+</sup> tILC in poly (I:C)-treated mice split into RORγt-FM<sup>+</sup> and RORγt-FM<sup>-</sup> cells. Two-tailed unpaired t-Test (**d**) or two-tailed Mann-Whitney Test (**j**).

Extended Data Figure 7. Disease-associated macrophage program in murine and human lupus nephritis. **a**, Gating strategy to identify kidney macrophages and monocytes by flow cytometry in nephritis. **b**, Quantification of blood monocytes (left to right: n = 4, 6, 4 mice per group). **c**, F4/80 (dark purple) and CD45*i.v.* (light teal) IF of kidney cortex, representative of n = 3, 4 mice per group. **d**, CD11b (dark purple) and CD45*i.v.* (light teal) IF of kidney cortex, images representative of 3 independent experiments. **e**, Fractions of M $\Phi$  subsets presented as percent of all immune cells within each of the indicated conditions. The bars show mean  $\pm$  SD (n = 3 mice per group). **f**, Pseudotime heatmap depicting expression of significant marker genes corresponding to three expression modules spanning the transition from monocyte (Mo) to M $\Phi$ . Annotations were colored by cell type, cell state and experimental groups (condition). Color scale indicates scaled marker gene expression across pseudotime. Representative genes included in each module are shown. **g**, Selected pathways regulated in M $\Phi$  and M $\Phi$ , in nephritis vs young mice. **h**, Matrix plot

indicating log2-transformed column scaled expression of exemplar genes selected from each module shown in f. i, Dot plot showing the expression levels of *Cfp* across whole kidney cell populations (left), or immune cell clusters (right). Dot size indicates percentage of expressing cells (% Exp.) and color scale shows average expression level of log-normalized counts (Avg Exp.). j, Violin plots of *C1QB*, *TREM2*, *APOE*, *LGMN* across leukocyte subpopulations. Subcluster analysis of 2,302 single-cell transcriptomes of human leukocytes isolated from 24 lupus nephritis patients and 10 controls.  $^{28}$  k, Top: representative images from CODEX analysis of kidney sections from young and nephritic mice. Bottom: Quantification of the location of CD206<sup>+</sup> macrophages in nephritic kidneys and young controls (top to bottom: n = 11, 11, 26, 8 visual fields for *young* and n = 17, 19, 23, 5 visual fields for *nephritis*). One-way ANOVA followed by Tukey's test (e) or Kruskal-Wallis test followed by Dunn's test (k).

Extended Data Figure 8. scRNA-seq analysis of leukocytes with and without aNKp46 and bulkRNA-seq of macrophage subsets. a, Left: Experimental set-up for scRNA-seq analysis of all immune cells minus tissue NKp46<sup>+</sup> ILC, isolated from 2 nephritic mice, and 3 mice treated anti-NKp46 blocking antibodies, related to b and Fig. 4f, g. Flow cytometry dot plots of kidney CD45<sup>+</sup> leukocytes. The red gates indicate NK1.1<sup>-</sup> leukocytes, as well as vessel-associated NK1.1<sup>+</sup> cells. The two populations were sequenced together. Right: UMAP embedding of 18,972 single-cell transcriptomes of kidney lymphocytes colored by Louvain clustering. Annotation to immune cell subpopulations was based on expression of canonical marker genes. MΦ, macrophage; Mo, Monocyte; cDC, conventional dendritic cell; T cell; PMN, polymorphonuclear neutrophils; Eos, eosinophils; B, B cell; UNO, unidentified cells. b, Dot plot of top 5 expressed genes across the kidney immune cell clusters shown in a. Dot size indicates percentage of expressing cells (% Exp.)

and color scale shows average expression level of log-normalized counts (Avg Exp.). **c**, Heat map showing levels of expression of selected genes in CD11b<sup>hi</sup> MHC2<sup>hi</sup> and CD11b<sup>hi</sup> MHC<sup>lo</sup> disease-associated macrophages and monocytes isolated from 3 nephritic mice vs CD11b<sup>lo</sup> MHC2<sup>hi</sup> tissue resident macrophages isolated from 3 young non-nephritic controls.

1258

1259

1260

1261

1262

1263

1264

1265

1266

1267

1268

1269

1270

1271

1272

1273

1274

1275

1254

1255

1256

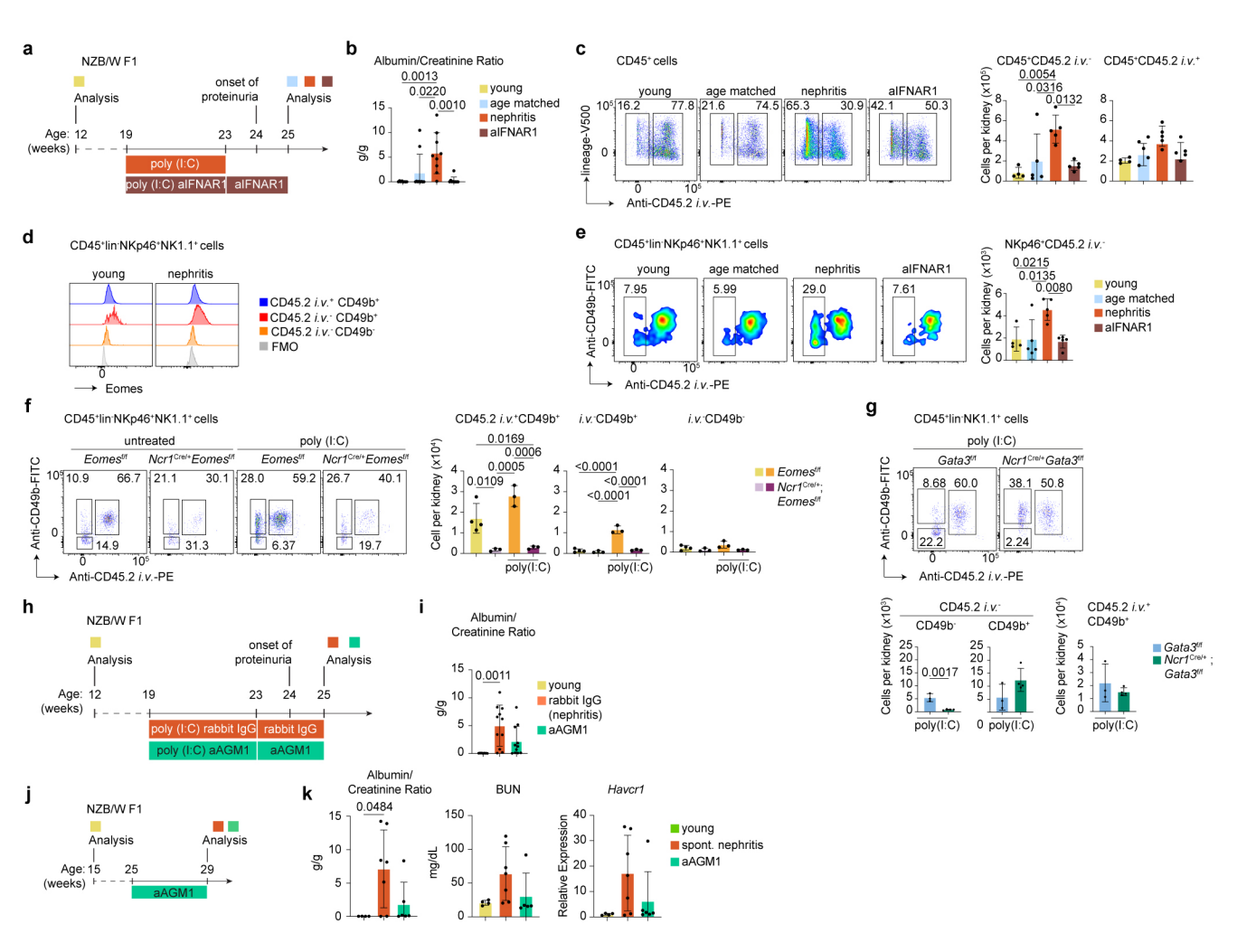
1257

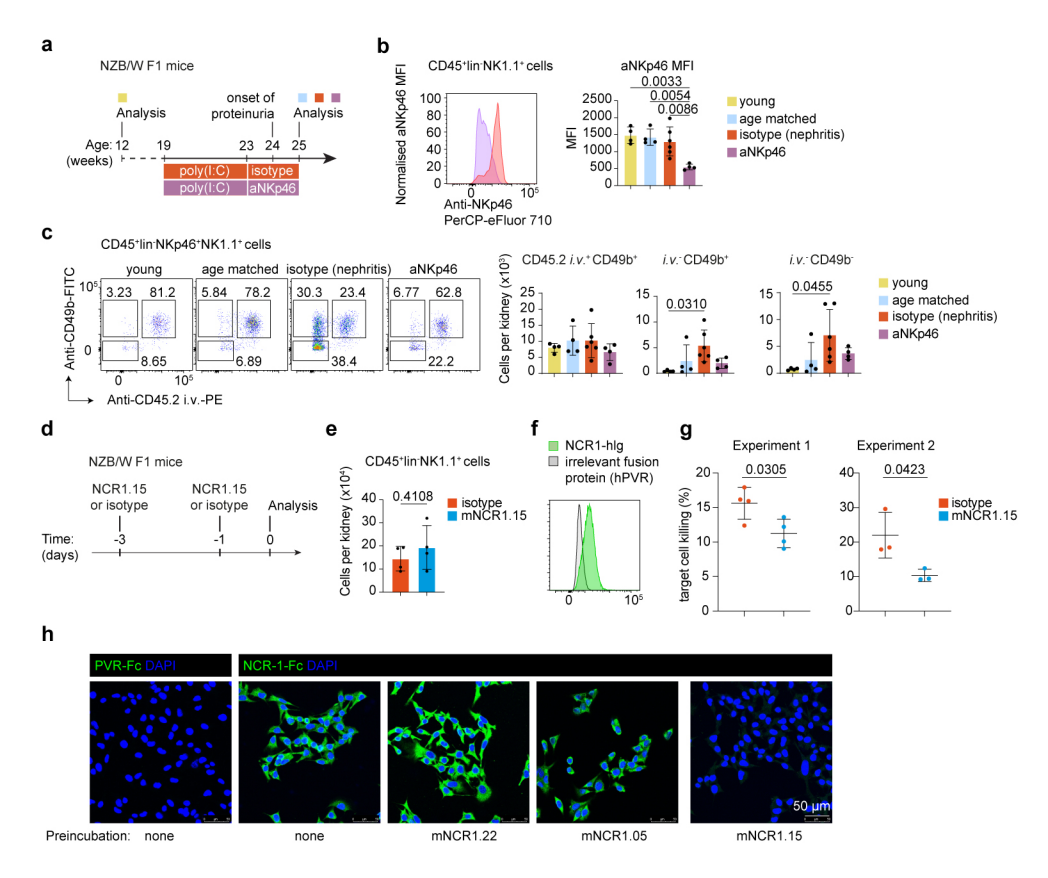
## Extended Data Figure 9. NKp46+ ILC control monocyte-derived MΦ via CSF2.

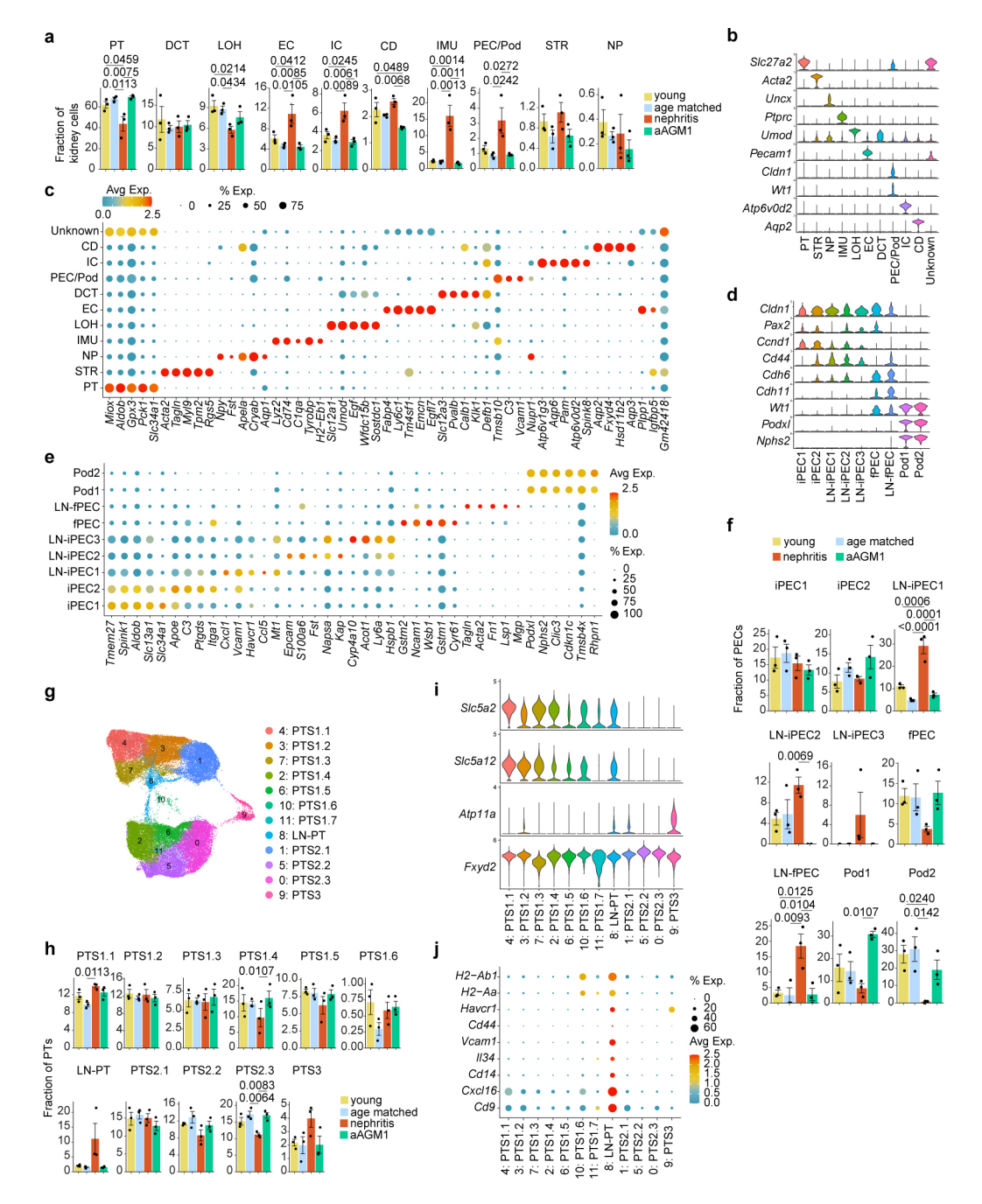
a, Experimental set-up to label longer-lived tissue macrophages followed by poly (I:C) treatment and isotype control or anti-CSF2 blocking antibodies, related to b. b, Right top: representative flow cytometry plots of kidney Lin<sup>-</sup> CD11b<sup>+</sup> cells stained for CD45i.v and F4/80. The gates indicate F4/80<sup>+</sup> CD45*i.v.*-/int MΦ. Right bottom: representative dot plots of F4/80<sup>+</sup> CD45*i.v.*-/int macrophages analyzed for F4/80 and CX3CR1-TdTomato. Left: Quantification of TdTomato and TdTomato<sup>+</sup> M $\Phi$  (left to right: n = 3, 4, 4 mice per condition). c, Top: Experimental set up to label blood derived cells 5 min and 12 hours prior to analysis, related to d, e. d, Top: Representative flow cytometry plots of kidney Lin<sup>-</sup>CD11b<sup>+</sup> cells that were either CD45i.v.<sup>-</sup> ('tissue cells') or were labeled positive with CD45i.v. injected 5min ('5min vessel-associated'), 5min and 12h ('12h vessel-associated'), 12h but not 5min ('recruited within 12h tissue cells') before analysis, analyzed for F4/80 expression. Bottom: Representative flow cytometry plots of kidney Lin<sup>-</sup>CD11b<sup>+</sup>F4/80<sup>-</sup> cells analyzed for Ly6C and CD43. e, Representative flow cytometry plots of kidney M $\Phi$ , analyzed for MHC2, CD11b and CD43. Data in d-e are representative of 3 nephritic mice. f, Experimental set up for anti-CSF1R treatment, related to g, and Fig. 5a, b. g, Quantification of the indicated monocyte subsets (left to right: n = 4, 6, 6 mice per group). h, Experimental Set-up for the analysis of B6.Sle1Yaa and B6.Sle1Yaa; Trem2-/- mice, related to i-j and Fig. 5d-e. i, Quantification of the indicated M $\Phi$  (i) and monocyte (j) subsets (left to right: n = 3, 12, 7 mice per group). One-way ANOVA followed by Tukey's test (**b**, **g**, **i**, **j**). The bars show mean  $\pm$  SD.

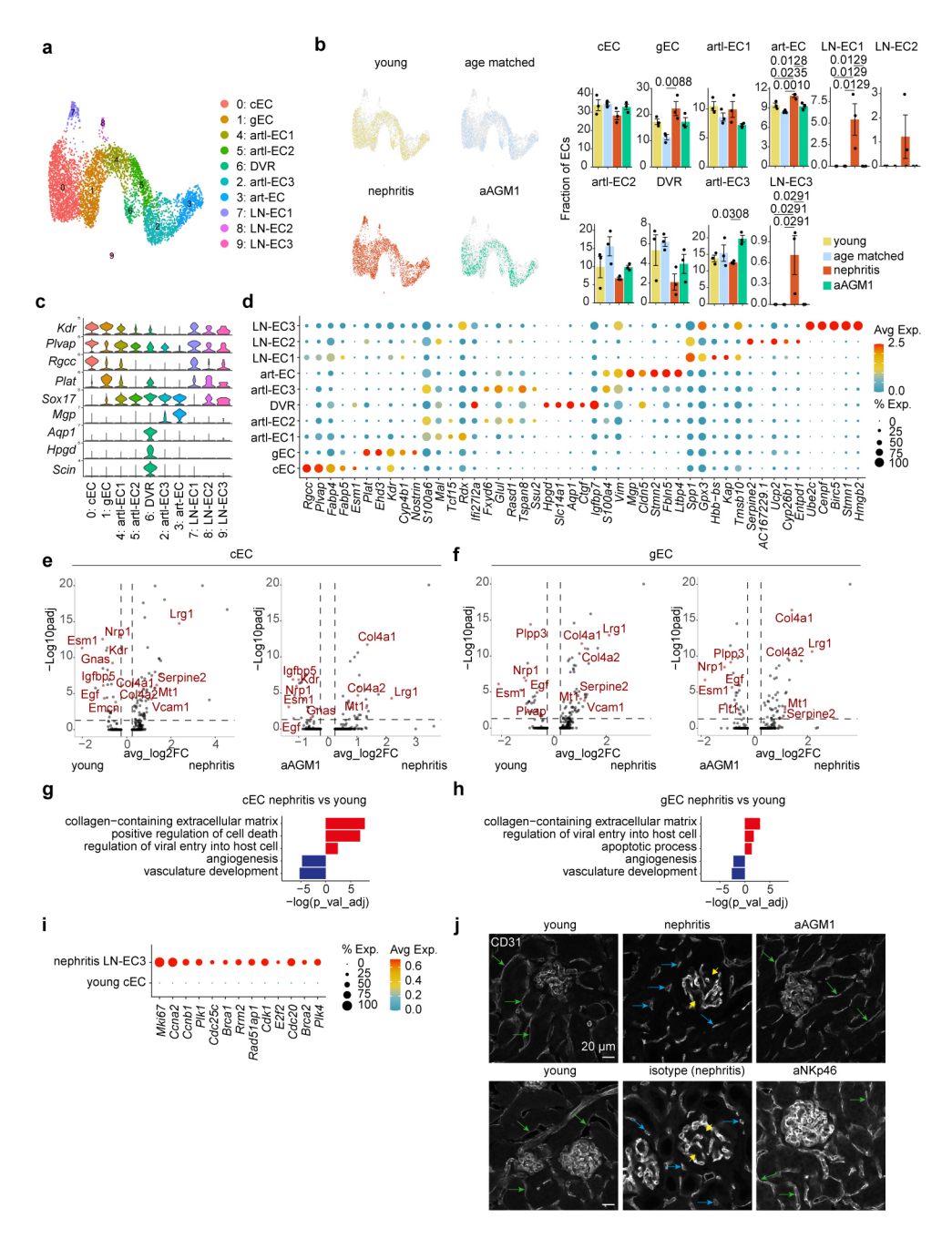
# Extended Data Fig. 10. Graphic Summary and Proposed Model

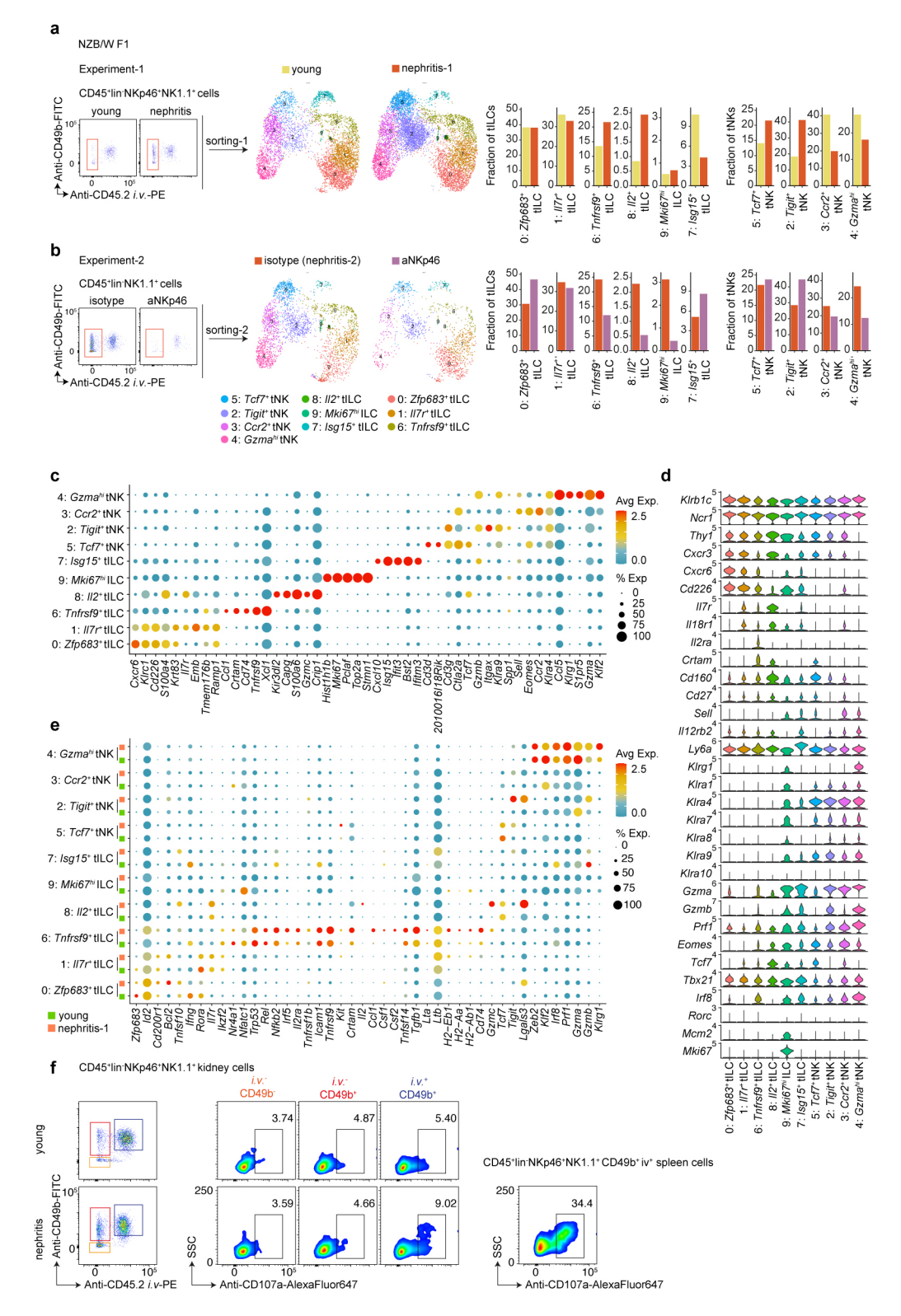
**a**, At homeostasis kidney tissue contains resident innate immune cells, including kidney tissue-resident ILC1 expressing NKp46, and kidney-resident macrophages, which at homeostasis are closely associated with capillary endothelial cells<sup>60</sup>. **b**, In autoimmunity, NKp46 may bind NKp46 ligands expressed by disease-associated macrophages, such as properdin<sup>37</sup>, a serum glycoprotein that activates the alternative complement pathway and that can bind to apoptotic cells. NKp46 activation induces the expression of immunoregulatory molecules, including CSF2, in a distinct subset of NKp46<sup>+</sup> tissue ILC, *Tnfrsf9*<sup>+</sup> ILC1. ILC1-derived CSF2 in turn promotes the population expansion of monocyte-derived, disease-associated macrophages that we link to epithelial cell damage and fibrosis. Prolonged monocyte-derived and kidney-resident macrophage interactions with activated injured epithelial cells lead to upregulation of TREM2, giving rise to TREM2<sup>hi</sup> disease-associated macrophages. **c**, Blocking of NKp46<sup>+</sup> ILC or genetic deficiency of NKp46 suppresses kidney CSF2, disease-associated macrophage population expansion and severe tissue damage. **d**, TREM2 signaling promotes anti-inflammatory macrophage states.

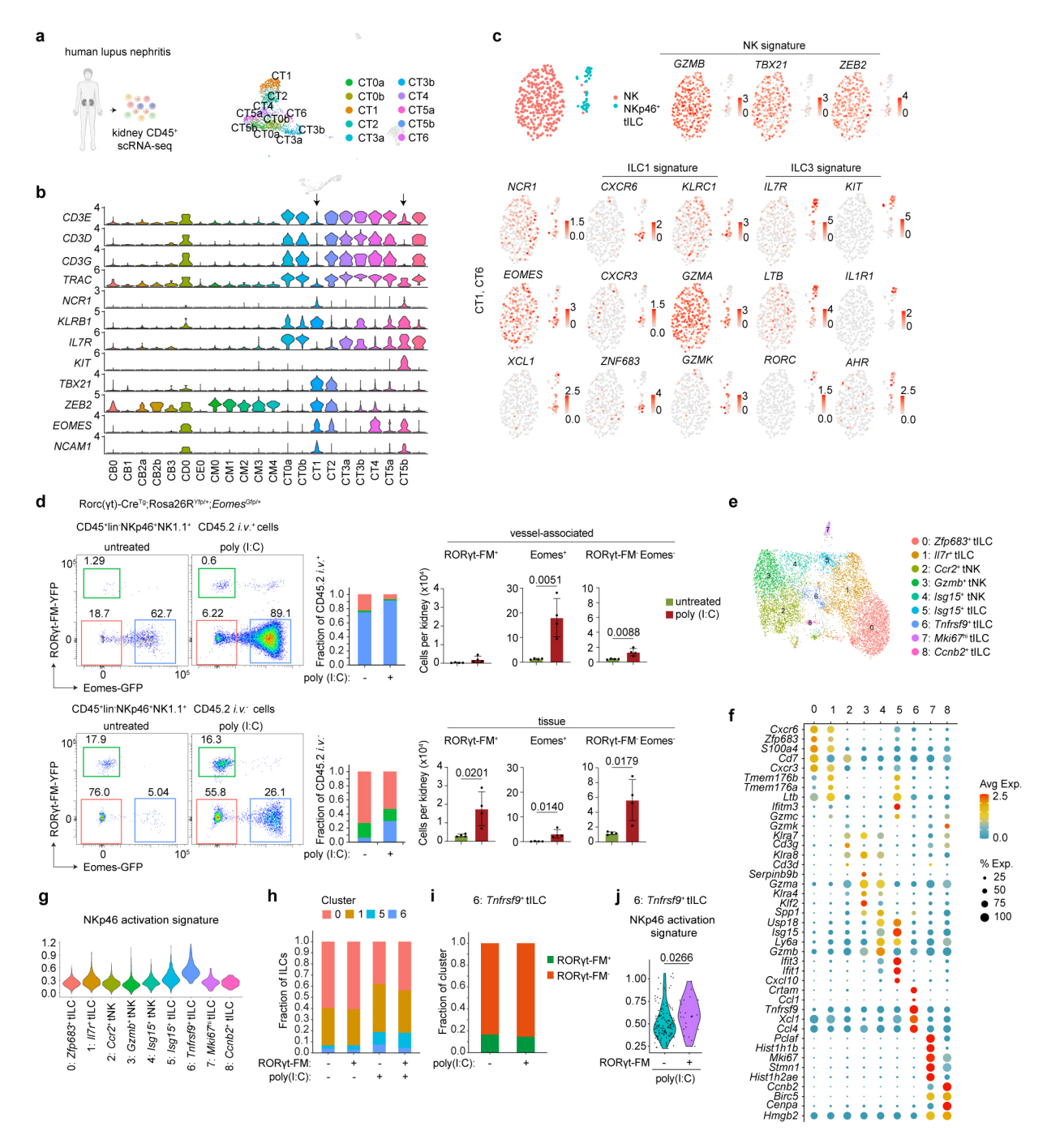


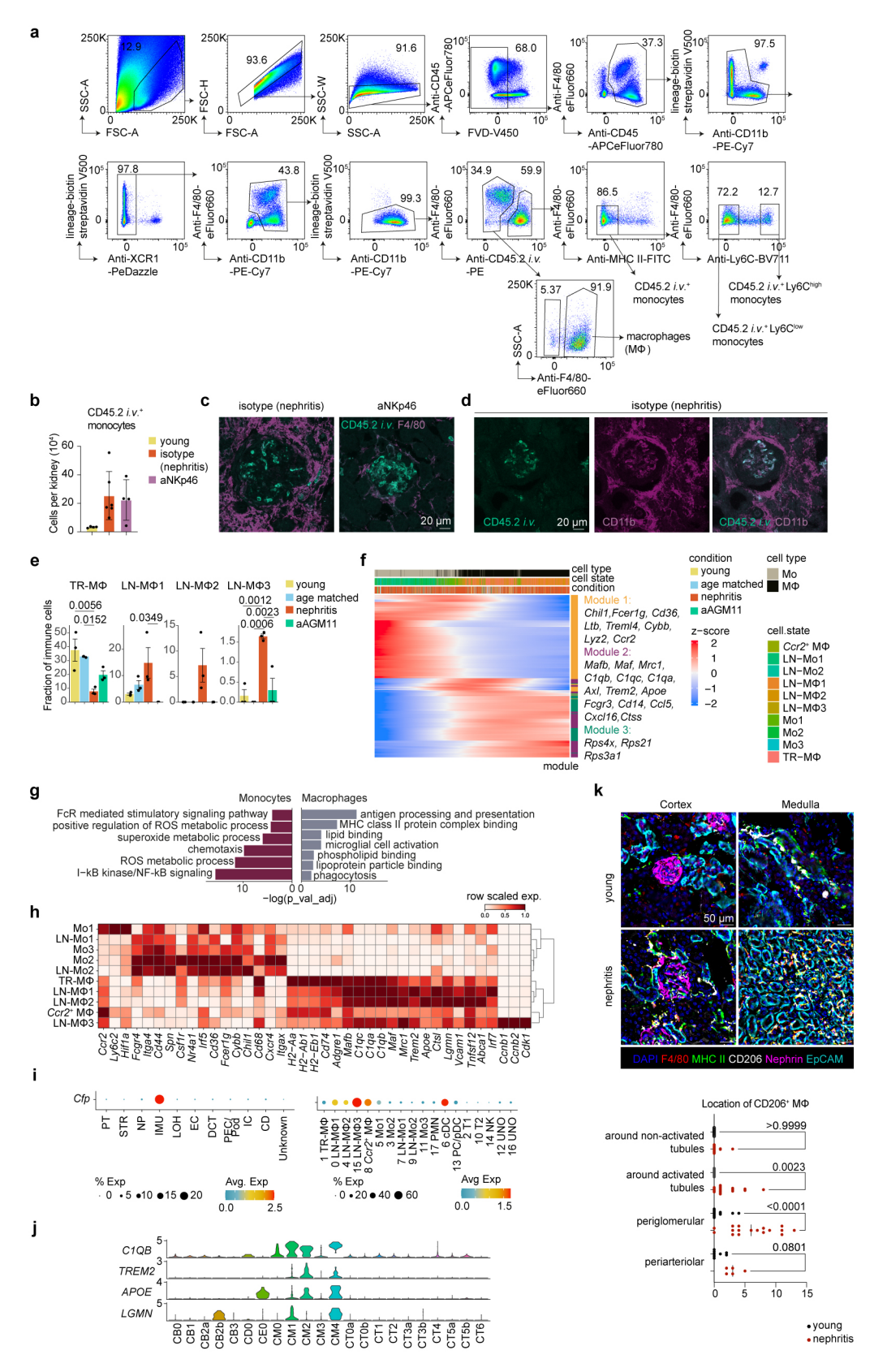


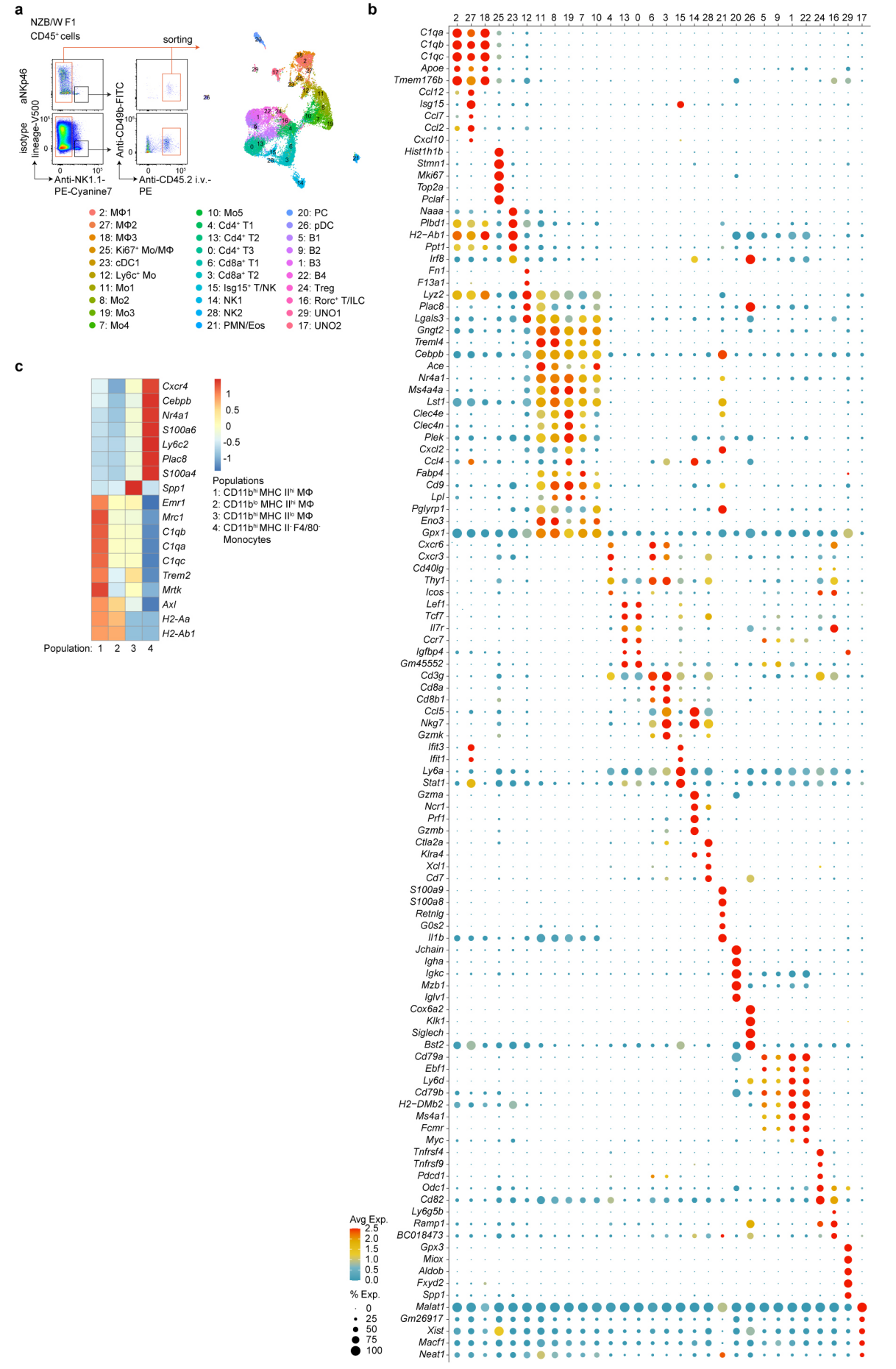


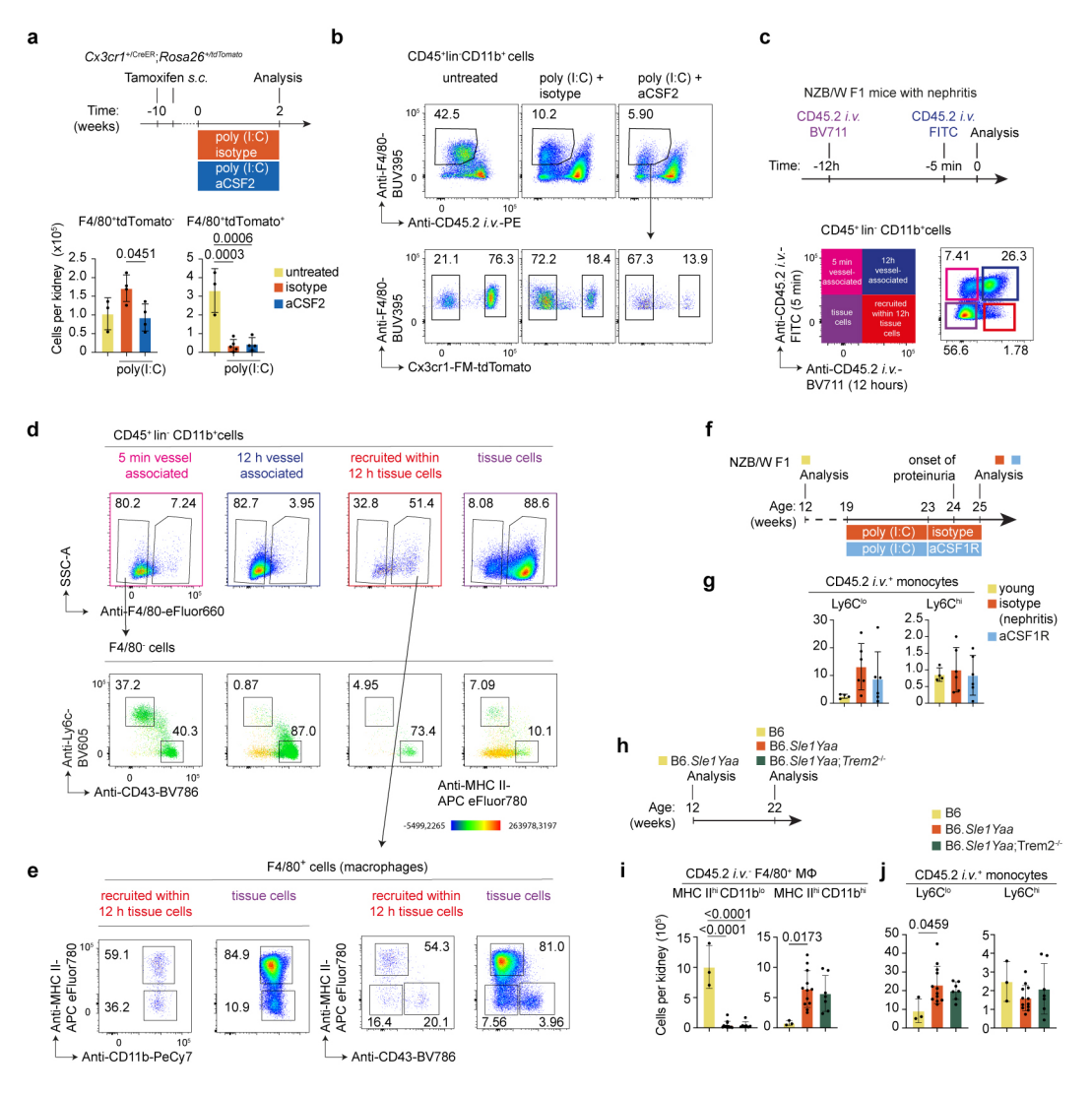


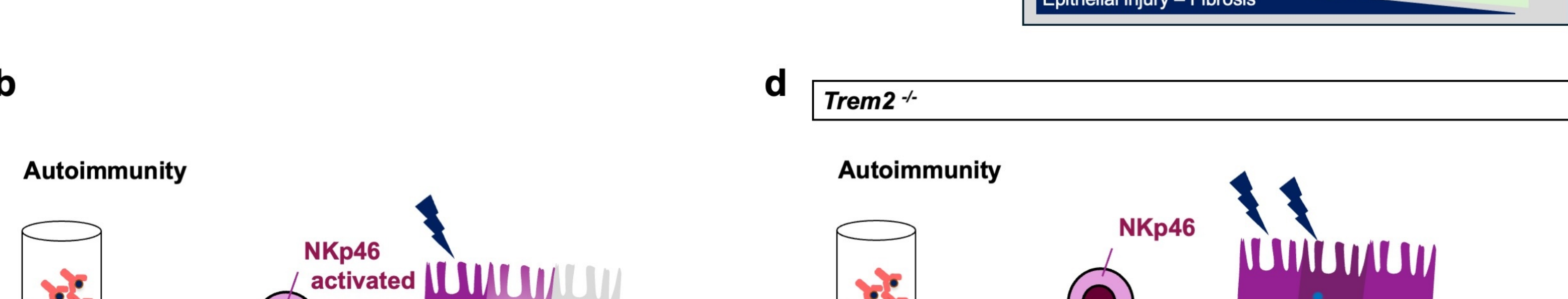












TREM2hi

injury repair

